


FULL PAPER

Open Access



# The spatial distribution of soluble organic matter and their relationship to minerals in the asteroid (162173) Ryugu

Minako Hashiguchi<sup>1\*</sup> , Dan Aoki<sup>2</sup>, Kazuhiko Fukushima<sup>2</sup>, Hiroshi Naraoka<sup>3</sup>, Yoshinori Takano<sup>4</sup>, Jason P. Dworkin<sup>5</sup>, Karin E. Dworkin<sup>6</sup>, José C. Aponte<sup>5</sup>, Jamie E. Elsila<sup>5</sup>, John M. Eiler<sup>7</sup>, Yoshihiro Furukawa<sup>8</sup>, Aogu Furusho<sup>9</sup>, Daniel P. Glavin<sup>5</sup>, Heather V. Graham<sup>5</sup>, Kenji Hamase<sup>9</sup>, Norbert Hertkorn<sup>10</sup>, Junko Isa<sup>11</sup>, Toshiki Koga<sup>4</sup>, Hannah L. McLain<sup>5,12</sup>, Hajime Mita<sup>13</sup>, Yasuhiro Oba<sup>14</sup>, Nanako O. Ogawa<sup>4</sup>, Naohiko Ohkouchi<sup>4</sup>, Francois-Regis Orthous-Daunay<sup>15</sup>, Eric T. Parker<sup>5</sup>, Alexander Ruf<sup>16,17,18</sup>, Saburo Sakai<sup>4</sup>, Philippe Schmitt-Kopplin<sup>10,19</sup>, Haruna Sugahara<sup>20</sup>, Roland Thissen<sup>21</sup>, Véronique Vuitton<sup>15</sup>, Cédric Wolters<sup>15</sup>, Toshihiro Yoshimura<sup>4</sup>, Hisayoshi Yurimoto<sup>22</sup>, Tomoki Nakamura<sup>8</sup>, Takaaki Noguchi<sup>23</sup>, Ryuji Okazaki<sup>24</sup>, Hikaru Yabuta<sup>25</sup>, Kanako Sakamoto<sup>20</sup>, Shogo Tachibana<sup>20,26</sup>, Toru Yada<sup>27</sup>, Masahiro Nishimura<sup>27</sup>, Aiko Nakato<sup>27</sup>, Akiko Miyazaki<sup>27</sup>, Kasumi Yogata<sup>27</sup>, Masanao Abe<sup>27</sup>, Tomohiro Usui<sup>27</sup>, Makoto Yoshikawa<sup>27</sup>, Takanao Saiki<sup>27</sup>, Satoshi Tanaka<sup>27</sup>, Fuyuto Terui<sup>28</sup>, Satoru Nakazawa<sup>27</sup>, Sei-ichiro Watanabe<sup>1</sup> and Yuichi Tsuda<sup>20</sup>

## Abstract

We performed *in-situ* analysis on a ~ 1 mm-sized grain A0080 returned by the Hayabusa2 spacecraft from near-Earth asteroid (162173) Ryugu to investigate the relationship of soluble organic matter (SOM) to minerals. Desorption electrospray ionization-high resolution mass spectrometry (DESI-HRMS) imaging mapped more than 200 CHN, CHO, CHO–Na (sodium adducted), and CHNO soluble organic compounds. A heterogeneous spatial distribution was observed for different compound classes of SOM as well as among alkylated homologues on the sample surface. The A0080 sample showed mineralogy more like an Ivuna-type (CI) carbonaceous chondrite than other meteorites. It contained two different lithologies, which are either rich (lithology 1) or poor (lithology 2) in magnetite, pyrrhotite, and dolomite. CHN compounds were more concentrated in lithology 1 than in lithology 2; on the other hand, CHO, CHO–Na, and CHNO compounds were distributed in both lithologies. Such different spatial distribution of SOM is likely the result of interaction of the SOM with minerals, during precipitation of the SOM via fluid activity, or could be due to difference in transportation efficiencies of SOMs in aqueous fluid. Organic-related ions measured by time-of-flight secondary ion mass spectrometry (ToF–SIMS) did not coincide with the spatial distribution revealed by DESI-HRMS imaging. This result may be because the different ionization mechanism between DESI and SIMS, or indicate that the ToF–SIMS data would be mainly derived from methanol-insoluble organic matter in A0080. In the Orgueil meteorite, such relationship between altered minerals and SOM distributions was not observed by DESI-HRMS analysis and field-emission scanning electron microscopy, which would result from differences of SOM formation processes and sequent alteration process on the parent bodies or even on the Earth. Alkylated homologues of CHN compounds were identified in A0080 by DESI-HRMS imaging as observed in the Murchison meteorite, but not from the Orgueil

\*Correspondence:

Minako Hashiguchi  
hashiguchi@eps.nagoya-u.ac.jp

Full list of author information is available at the end of the article

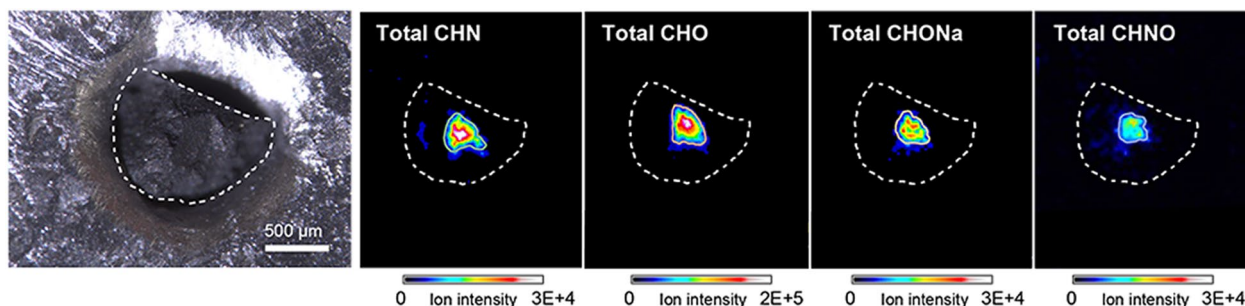


© The Author(s) 2023. **Open Access** This article is licensed under a Creative Commons Attribution 4.0 International License, which permits use, sharing, adaptation, distribution and reproduction in any medium or format, as long as you give appropriate credit to the original author(s) and the source, provide a link to the Creative Commons licence, and indicate if changes were made. The images or other third party material in this article are included in the article's Creative Commons licence, unless indicated otherwise in a credit line to the material. If material is not included in the article's Creative Commons licence and your intended use is not permitted by statutory regulation or exceeds the permitted use, you will need to obtain permission directly from the copyright holder. To view a copy of this licence, visit <http://creativecommons.org/licenses/by/4.0/>.

meteorite. These compounds with a large C number were enriched in Murchison fragments with abundant carbonate grains. In contrast, such relationship was not observed in A0080, implying different formation or growth mechanisms for the alkylated CHN compounds by interaction with fluid and minerals on the Murchison parent body and asteroid Ryugu.

**Keywords** Ryugu, Hayabusa2, Spatial distribution of soluble organic compounds, DESI-HRMS imaging, ToF-SIMS analysis

### Graphical Abstract



### Introduction

Recent non-targeted analyses using high-resolution mass spectrometry (HRMS) (Schmitt-Kopplin et al. 2010; Naraoka et al. 2017) has found high diversity and complexity of soluble organic materials (SOMs) in carbonaceous chondrites (CCs). Such extraterrestrial SOMs are expected to record the chemical evolution of the solar system from the presolar molecular cloud phase to present geological activities as well as prebiotic evolution of organics.

The Hayabusa2 spacecraft collected samples from two touchdown sites on C-type asteroid (162173) Ryugu and returned them to Earth on December 6, 2020 (Tachibana et al. 2022). One of the science goals is to understand the role of C-type asteroids on delivery of water and organic matter to the proto-Earth (Tachibana et al. 2014; Watanabe et al. 2017; Tachibana 2021). Initial spectroscopic investigation of returned samples with *MicrOmega*, a hyperspectral microscope, in the clean chamber at the JAXA curation facility, showed C–H vibration features of organic matter in the near-infrared wavelength range (Pilorget et al. 2021). *MicrOmega* found heterogeneity in spectroscopic features at submillimeter scale, and one particle potentially enriched in N–H bond was reported (Pilorget et al. 2021). Chemical, isotopic, and mineralogical or petrological analyses of asteroid Ryugu samples have similar characteristics as those of Ivuna-type (CI) CCs (Yada et al. 2021; Nakamura et al. 2022; Yokoyama et al. 2022). Organic analysis was performed for SOM and insoluble organic matter (IOM), revealing a high

variety of organic compounds as well as chemical and isotopic heterogeneities of organic matter from Ryugu grains (Naraoka et al. 2023; Yabuta et al. 2023). The solvent extracts from Ryugu aggregate sample A0106, collected at the first of two touchdown sites, showed a high molecular diversity consisting of C, H, N, O and/or S compositions by HRMS analysis, including the high abundance of poly-sulfur bearing species (Naraoka et al. 2023). Various soluble organic compounds including aliphatic amines, carboxylic acids, polycyclic aromatic hydrocarbons, amino acids, and alkylated N-bearing heterocyclic compounds were also detected (Aponte et al. 2023; Naraoka et al. 2023; Parker et al. 2023).

Macromolecular organic matter with complex structure and various morphology is ubiquitously present in Ryugu samples (Yabuta et al. 2023). Several functional groups, such as C=O, C=C, and Si–O, were assigned by micro-Fourier transform infrared spectroscopy ( $\mu$ -FTIR) and atomic force microscope-based infrared spectroscopy (AFM-IR) on the intact grains A0108 and C0109, which were from the first and second touchdown sites, respectively. These microscopic analyses also showed the close association of macromolecular organics with mineral components in the grains (Yabuta et al. 2023) as observed in CCs (Pearson et al. 2002; Kebukawa et al. 2010; Le Guillou et al. 2014; Noun et al. 2019).

The isotopic analysis revealed that the distributions of D/H ratio of Ryugu IOM were within the range of CI, Mighei-type (CM), and ungrouped Tagish Lake CCs, whereas the  $^{15}\text{N}/^{14}\text{N}$  ratio was only similar to that of CI

CCs (Yabuta et al. 2023). Furthermore,  $^{13}\text{C}$ -rich presolar grains were identified in Ryugu grains and their abundance was identical to that for CI, CM and CR CCs (Barosch et al. 2022; Yabuta et al. 2023). These results also suggest a potential Ryugu-CI CC connection. Furthermore, the presence of isotope heterogeneity in Ryugu organic matter suggests the characteristics of organics in the preaccretion phase was not completely erased by parent body alteration processes.

We recently reported the heterogeneous distribution of soluble organic compounds in Ryugu grains by desorption electrospray ionization (DESI) technique coupled with HRMS (Naraoka et al. 2023). In this study, we further reveal the association of organic matter with minerals on Ryugu. We performed *in-situ* analysis of SOMs on an intact Ryugu sample using desorption electrospray ionization (DESI) technique coupled with HRMS (Naraoka and Hashiguchi 2018; Hashiguchi and Naraoka 2019a, 2019b; Naraoka et al. 2023) and time of flight-secondary ion mass spectrometry (ToF-SIMS), and mineralogical observation to investigate the relationship of organic compounds and minerals.

### Sample and experiments

The grain (A0080) used in this study, collected at the first touchdown site on 21 February 2019 from the surface of Ryugu, has a flat surface and  $\sim 1$  mm in size (Additional file 1: Fig. S1). Because of its fragile nature, the grain was embedded in a soft alloy of Bi, Sn, and In (U-alloy, U-49 (the melting point: 49 °C); Osaka Asahi Co., Ltd.) without any brazing or polishing (Fig. 1a). Organic molecular imaging was performed on a 2.8 mm  $\times$  2.8 mm area of the sample surface including surrounding metal, which was used for a blank, using DESI-HRMS system, which is a 2D-DESI ion source (Omni Spray Source 2D, Prosolia Inc.) equipped with a hybrid quadrupole-Orbitrap mass spectrometer (Q-Exactive Plus, Thermo Fisher Scientific) at Kyushu University. The spray solvent was 100% methanol (FUJIFILM Wako Pure Chemical Corporation, LC-MS grade) with a flow rate of 3  $\mu\text{l}/\text{min}$ . The spot size was  $\sim 150$   $\mu\text{m}$  and spatial resolution is approximately 100  $\mu\text{m}$  estimated using Rhodamine B on a single Teflon coated spot on a standard Prosolia Omni Slide<sup>TM</sup>. The desorbed positive ions ( $m/z$  50–500) were collected in full scan mode with a mass resolution of 140,000 ( $m/\Delta m$  at  $m/z = 200$ ). During the imaging, a lock mass mode was employed to calibrate the accurate mass using dioctyl phthalate ( $[\text{C}_{24}\text{H}_{38}\text{O}_4 + \text{H}]^+ = 391.2843$ ) derived from polyether ether ketone (PEEK) tubing attached to a fused silica capillary for solvent spray. Other detailed analytical conditions are described in Naraoka and Hashiguchi (2018) and Hashiguchi and

Naraoka (2019b). The criterion for identification of mass peaks from the sample surface was the intensity ratio  $> 10$  at the sample surface (inside of the dotted line in Fig. 1b) to the outside, which contained background ions from spray solvent and/or surrounding air. The obtained mass spectral data were converted to a text data file for imaging by Firefly software (Prosolia Inc.) and the DESI images were visualized using BioMAP (maldi-msi.org). For the image analysis, the mass resolution of  $m/z$  of  $\pm \sim 0.001$  was adapted. The chemical formulae of identified peaks were assigned using  $^{12}\text{C}$ ,  $^{13}\text{C}$ , H,  $^{14}\text{N}$ ,  $^{16}\text{O}$ ,  $^{23}\text{Na}$ , and  $^{32}\text{S}$ , then filtered by  $\pm 3$  ppm mass precision, that is defined as  $[(\text{measured } m/z) - (\text{calculated } m/z)]/(\text{calculated } m/z) - 1 \times 10^6$  (ppm).

After the imaging, the ToF-SIMS measurement was performed on the same surface of A0080 using a TRIFT III spectrometer (ULVAC-PHI, Inc.) at Nagoya University. Positive and negative spectra were obtained using an  $\text{Au}^+$  beam. An accelerating voltage and current of the primary ion were 22 kV and 2.6 nA, respectively. The ion beam pulse width was set at 1.4 ns (bunched mode) and 9.5 ns (non-bunched mode) for spectral and image analysis, respectively. The angle between the primary  $\text{Au}^+$  ion beam and the sample surface was 40°. The beam size was estimated to be  $\sim 1$   $\mu\text{m}$  and surface areas of 100  $\times$  100 to 150  $\times$  150  $\mu\text{m}$  were measured. Approximately  $10^7$  total ion counts were obtained in acquisition time of about 5 min. A low-energy pulsed electron ion gun of 28.0 eV was used for surface charge compensation.

After the ToF-SIMS analysis, detailed mineralogical observation of the grain surface was performed using a field-emission scanning electron microscope (FE-SEM) (Hitachi, SU 6600) equipped with energy dispersive X-ray spectroscopy (EDS) (HORIBA, EMAX Energy) at Nagoya University using an accelerating voltage of 10 kV. The topography of the sample surface was also observed using a laser scanning microscope (Nikon Instruments Inc., A1RMP) equipped with a 10 $\times$  objective lens at Nagoya University Equipment Sharing System. A laser at 405 nm wavelength was used and the topography was measured using a step of  $\sim 1$   $\mu\text{m}$ .

We also analyzed an antigorite grain as a procedural blank in the series of analyses (DESI-HRMS and ToF-SIMS), which was heated in air at 450 °C for 3 h and then methanol washed and studied using the same methods as described above. Orgueil and Murchison CC fragments were analyzed by DESI-HRMS using methanol spray of 2–3  $\mu\text{l}/\text{min}$  for comparison. The Ryugu grain and the blank sample were stored in a pure  $\text{N}_2$ -purged container or sealed glass vial for blank and meteorite sample during transportation between institutes.

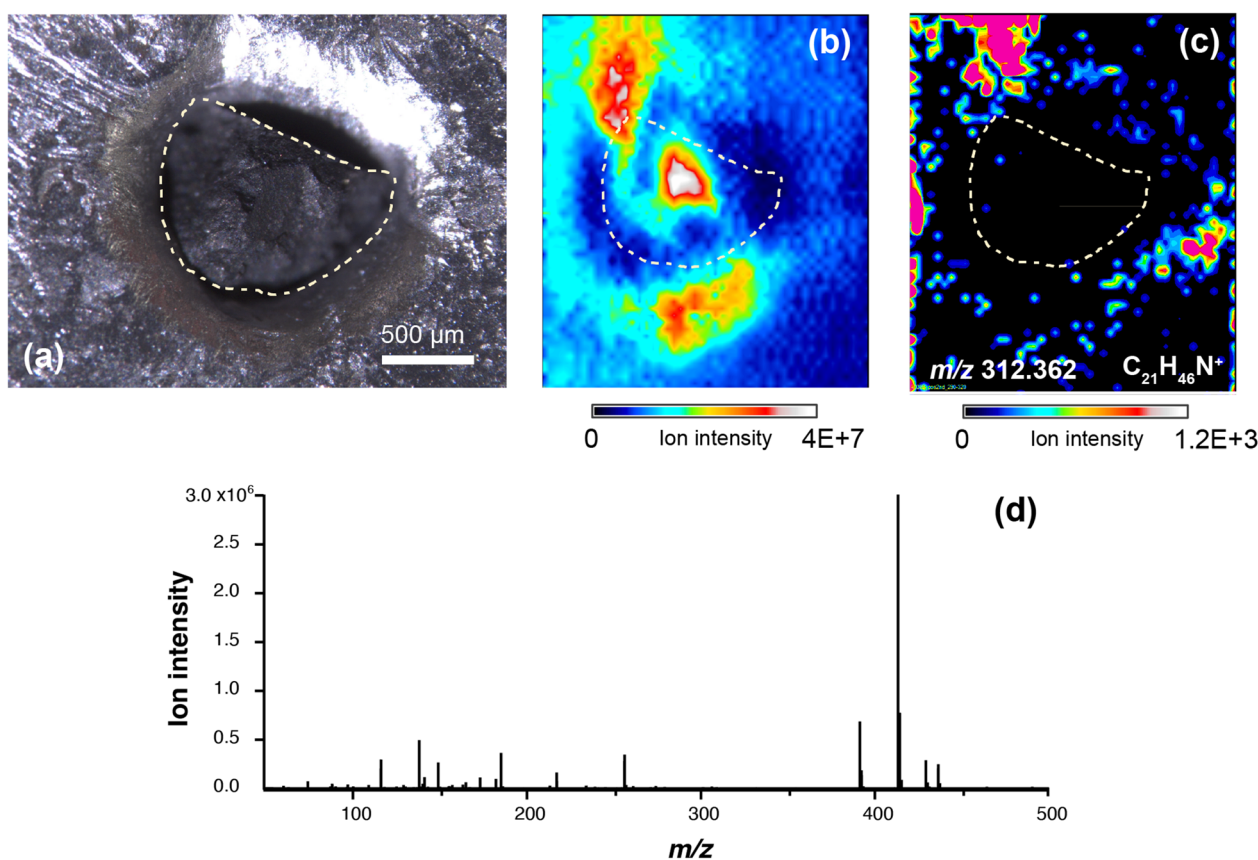


**Fig. 1** **a** An optical microscope image of A0080. The dotted line represents the outline of A0080, which was embedded in a soft alloy. **b** A total ion image obtained by DESI-HRMS. **c** A mass spectral image of  $C_{21}H_{46}N^+$  ( $m/z$  312.362). **d** A mass spectrum of total ion obtained from the entire surface of the grain, inside of the region of interest (ROI) indicated by the dotted line in (a)–(c)

Data analysis was performed using Image J and Adobe Photoshop for DESI-HRMS imaging and FE-SEM data and Wincadence software (Ulvac-phi. Inc) for ToF-SIMS data.

## Results

### Organic compound species identified by *in-situ* DESI-HRMS analysis of A0080

A set of optical, total ion, and specific ion images of A0080 are shown in Fig. 1 with a mass spectrum obtained from the entire grain surface. Ion signals were observed both from the sample surface and its outside. Peaks detected from outside the sample came from surrounding metal and/or surrounding air. For instance, an ion of  $m/z$  312.362 ( $C_{21}H_{46}N^+$ ; Fig. 1c) was detected only from the surrounding metal alloy and should not be indigenous to A0080.

More than 200 positive ions were identified in  $m/z$  80–400 from the grain surface of A0080 by DESI-HRMS imaging and assigned to CHN, CHO, CHO–Na, and CHNO compounds within  $\pm 3$  ppm in mass precision.

Sulfur-bearing species, which are abundantly present in Ryugu SOMs (Naraoka et al. 2023), were not identified likely because the DESI imaging was made for positive ions.

The CHO compounds were dominated among the identified species both in terms of signal intensity ( $\sim 65\%$  of the total ion counts) and number (Fig. 2a; Table 1). The CHN, CHO, CHO–Na, and CHNO compounds include their  $CH_2$  alkylated homologues such as  $C_nH_{2n+2}N^+$ ,  $C_nH_{2n-4}N^+$ , and  $C_nH_{2n-1}N_2^+$  for CHN ( $n=4$  to 22),  $C_nH_{2n-8}O_4^+$ ,  $C_nH_{2n}O_4^+$ , and  $C_nH_{2n+2}O_5^+$  for CHO ( $n=4$  to 16) (Table 2). The abundant  $CH_2$  homologs of CHN compounds were also identified from analysis of solvent extracts from CCs (Naraoka et al. 2017; Isa et al. 2021) and Ryugu grain A0106 (Naraoka et al. 2023, Oba et al. 2022, Oba et al. 2023) and *in-situ* DESI imaging of CCs (Naraoka and Hashiguchi 2018; Hashiguchi and Naraoka 2019b).

In contrast to the presence of Mg-containing metalorganic compounds in several CCs including Murchison and Tagish Lake (Ruf et al. 2017; Hashiguchi and Naraoka 2019a), the Mg-containing organic species were not

detected from A0080. Among these identified organic species, a total of 35% of them (78% of CHN compounds, 11% of CHO compounds, 52% of CHNO compounds, and 7% of CHO–Na compounds, respectively) were reported as positive ions in the methanol extract of the Ryugu aggregate sample (A0106) using nano-liquid chromatograph (nano-LC) equipped with a nano-electrospray ionization (ESI) and nanoAmide column (Naraoka et al. 2023), while others are newly identified in this work.

#### Spatial distribution of SOM related to mineralogy of A0080

The detected organic ions are heterogeneously distributed on the sample surface and are concentrated in specific regions on the surface. The grain surface after the DESI-HRMS imaging appeared rougher than the original surface and had up to about 150  $\mu\text{m}$  of roughness (Additional file 1: Fig. S2). This is because of the loss of small fragments from the surface by the spraying of methanol solvent and/or  $\text{N}_2$  gas used for the DESI system. The distribution of ion signals was affected by the surface roughness and were generally highest around the highest region of the grain surface (Additional file 1: Fig. S2). Despite the roughness effect on ion detection, total ion signals of CHN, CHO, CHO–Na, and CHNO compounds showed different spatial distributions on the sample surface (Fig. 2b). For example, most of the CHN compounds appear to be concentrated in the lower region of the sample surface shown in Fig. 2b relative to CHO compounds that are concentrated in the upper region. CHNO and CHO–Na compounds were detected in the intermediate region. In DESI-HRMS imaging with the same conditions of analysis on A0080 (spot size of spray solvent of 150  $\mu\text{m}$ , and scan rate of around 65 m/s for  $x$  axis), a difference of 70  $\mu\text{m}$  in depth reduces the ion intensity by about 50% (Additional file 1: Fig. S3). However, the reduction of ion intensity was not significantly different between a depth difference of 70  $\mu\text{m}$  and 90  $\mu\text{m}$  if the width of the step is less than 250  $\mu\text{m}$  (Additional file 1: Fig. S3). The SOM concentrated region in A0080 is a matrix region composed of submicron-scale particles with a maximum roughness of about 70  $\mu\text{m}$  and no deep steps with a width exceeding 90  $\mu\text{m}$ . The analyses were performed simultaneously under the same conditions for identification of all SOM compounds, therefore the differences in the spatial distribution of those SOM by different chemical composition do not reflect sample roughness.

FE-SEM–EDS analysis showed that A0080 consists mainly of phyllosilicates, magnetite, pyrrhotite, and dolomite grains larger than 10  $\mu\text{m}$  in size. Although breunnerite, dolomite and calcite were observed in Ryugu samples (Kawasaki et al. 2022; Nakamura et al. 2022; Yokoyama et al. 2022; Loizeau et al. 2023), carbonates observed

in A0080 were almost dolomite. Further, there are two distinct lithologies in A0080; one is enriched in large (>10  $\mu\text{m}$ ) magnetite, pyrrhotite, and carbonate (dolomite) grains (lithology 1) and the other is poor in those minerals (lithology 2) (Figs. 3a–c). There were neither chondrules nor Ca–Al-rich inclusions (CAI) observed on the A0080 surface. In both lithologies, magnetite showed various morphologies, such as single hexagonal crystals and spherical (including framboids for magnetite) and screw-shaped crystals called plaquettes (Figs. 3e, f) (Kimura et al. 2013; Gounelle and Zolensky 2014). Pyrrhotite also occurs as a single hexagonal crystal, which is up to ~30  $\mu\text{m}$ , and irregular or spherical shape (Figs. 3e, f). The textures of magnetite and pyrrhotite in A0080 were similar to those in CI CCs (Gounelle and Zolensky 2014). Such mineralogical and petrological features of A0080 are similar to that of the most common lithology in Ryugu grains (Nakamura et al. 2022; Yokoyama et al. 2022).

In the high SOM signal region of the grain, the CHO compounds are distributed in both lithology 1 and 2, while CHN, CHO–Na, and CHNO compounds were enriched in smaller regions, especially in lithology 2 (Figs. 3a–d, 4). Furthermore, the spatial distribution of each species was different among the same alkyl homologues (Fig. 5) of these CHN, CHO, and CHNO compounds. Figure 6 shows the ion intensity ratio of the alkyl homologues with different sizes from lithology 1 (region of interest, ROI 1) to lithology 2 (ROI 2). There were no clear correlations in abundances of CHN, CHO, CHNO, and CHO–Na compound groups between the two different ROIs and the amount of alkylation in the same  $\text{CH}_2$  homologues (Figs. 6b–d).

#### ToF–SIMS analysis

Ion images obtained by ToF–SIMS after DESI–HRMS analyses showed heterogeneous distributions of both inorganic and organic ions (Additional file 1: Fig. S4). The spatial distributions of inorganic elements ( $\text{Si}^+$ ,  $\text{Mg}^+$ , and  $\text{Fe}^+$ ) were very similar to each other, suggesting that the image heterogeneity reflected the roughness of the sample surface rather than the mineral distribution (e.g., pyrrhotite and magnetite) as shown in previous studies of ToF–SIMS analysis on CCs (Noun et al. 2019). The ToF–SIMS data obtained in spectral mode were used to compare the abundances of organic-related ions, including positive ions ( $^{12}\text{C}^+$ ,  $^{12}\text{CH}_2^+$ ,  $\text{C}_3\text{H}_9^+$ ,  $\text{CNO}^+$ , and  $\text{CNNO}^+$ ) and negative ions ( $\text{CH}^-$ ,  $\text{CN}^-$ ,  $\text{CO}_2^-$ ,  $\text{CO}_3^-$ ,  $\text{CO}_4^-$ , and  $\text{C}_3\text{H}_9^-$ ), in three regions; Area A (enriched in CHN, CHO, CHO–Na, and CHNO), area B (boundary of CHO-rich and CHNO/CHN-poor region), and area C (CHO-rich and CHNO/CHN-poor region) were identified

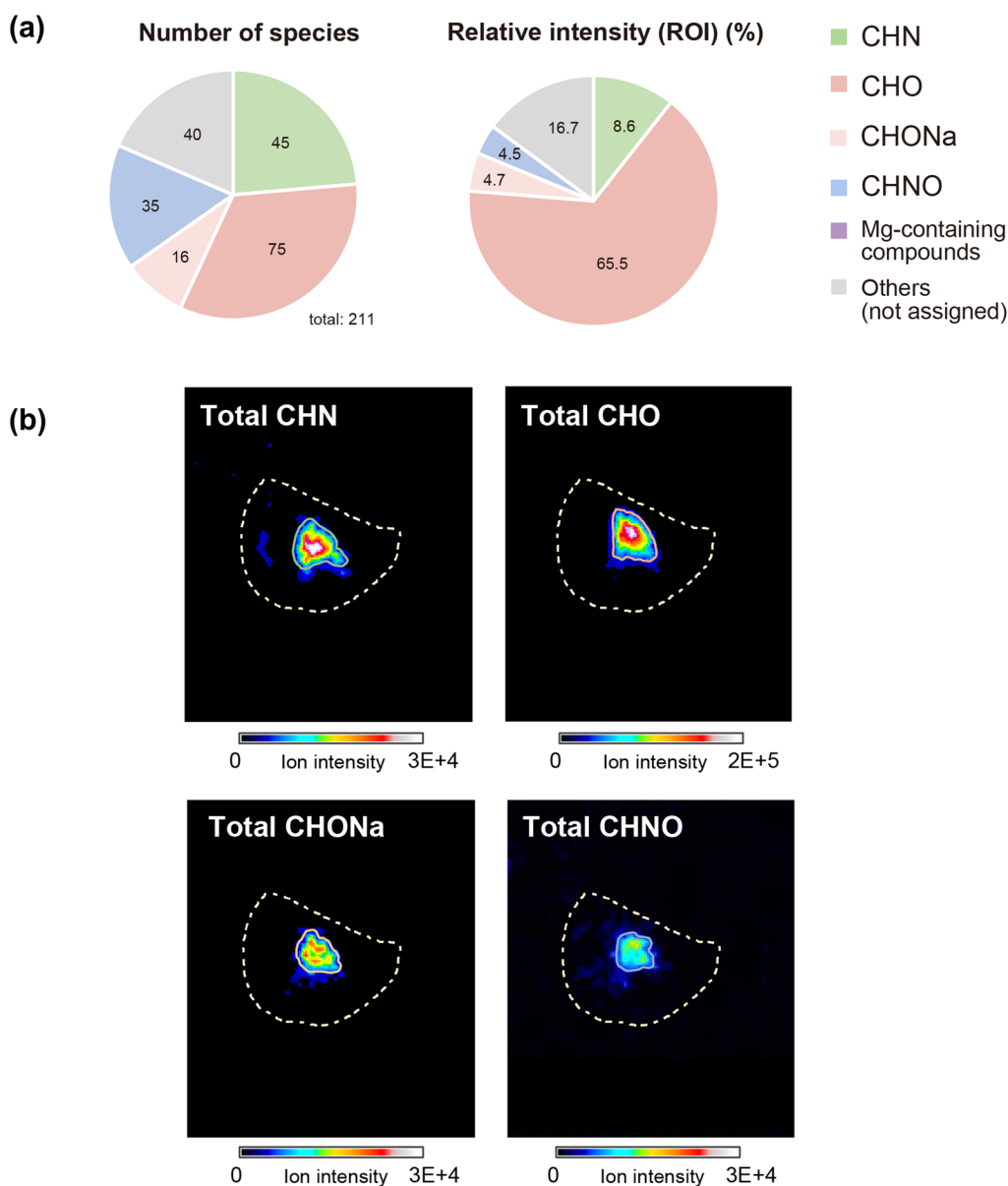


**Fig. 2** **a** The number of species and the relative intensity (%) of identified compounds from A0080. The relative intensity was calculated using total intensity from ROI (inside of the dotted line, corresponding to the sample surface of A0080). **b** DESI-HRMS images of total ions of CHN, CHO, CHO–Na, and CHNO compounds, respectively. Outlines in these images for each compound correspond to >40% of maximum ion intensity

by DESI-HRMS imaging and FE-SEM observations (Fig. 7). The  $\text{CNO}^+$  and  $\text{CNNO}^+$  ions detected by ToF–SIMS were more abundant in the CHO-rich and CHNO/CHN-poor region that was identified by DESI-HRMS imaging (area C > area B > area A). The intensities of  $^{12}\text{C}^+$  ions were almost similar in the three areas. Negative ions  $\text{CN}^-$ ,  $\text{CO}_3^-$  and  $\text{CO}_4^-$  also showed similar trends to  $\text{CNO}^+$  and  $\text{CHNO}^+$  (Figs. 7b, c). In contrast,  $\text{CO}_2^-$  and  $\text{C}_3\text{H}_9^-$  were less in area B than in areas A and C.

#### Comparison for spatial compound distribution in the Orgueil and Murchison meteorites

About 80 and about 400 compounds were identified from Orgueil and each of two Murchison fragments (fragment 1 and 2) by DESI-HRMS imaging using methanol spray, respectively (Fig. 8; Table 1). These compounds were assigned to CHN, CHO, CHO–Na, and CHNO compound groups based on their molecular compositions. For Orgueil, CHO compounds were most abundant (~40%) and CHO–Na compounds show the highest ion

**Table 1** Identified species from the sample by methanol-sprayed DESI-HRMS imaging

	CHN	CHO	CHO-Na	CHNO	MgOC*	Unassigned	Total
<i>A0080</i>							
Species	45	75	16	35	n.d	40	211
Intensity (%)	8.5	65.6	4.7	4.5	n.d	16.7	100
<i>Orgueil</i>							
Species	3	33	16	7	64	25	84
Intensity (%)	0.1	29.3	41.1	7.3	n.d	22.2	100
<i>Murchison fragment 1</i>							
Species	143	21	5	107	64	59	399
Intensity (%)	5.6	7.2	3.6	75.2	4.0	4.4	100
<i>Murchison fragment 2</i>							
Species	158	28	5	96	64	60	411
Intensity (%)	4.2	6.1	3.3	81.1	2.1	3.2	100

\* MgOC: Mg-containing organic compounds

intensities (~41%) (Fig. 8c). Very few CHN compounds were identified. For both fragments of Murchison meteorites, CHNO compounds were the most abundant relative intensities (75–80%), although CHN compounds were the most in the number of species. The CHN compounds in Murchison include 13 suites of alkyl homologues, which are more abundant than those in A0080. Even though some CHNO species were identified as alkyl homologues, most CHNO species have no alkyl homologues. A small abundance of alkyl homologues of CHO and CHO–Na was identified in Murchison (Table 2); in contrast they are abundant in the Orgueil meteorite similar to A0080. The total ion of CHN, CHO, CHO–Na, and CHNO groups showed different spatial distributions in the sample surfaces (Fig. 9). Alkyl homologues of CHN compounds showed different ion intensities but similar spatial distributions in the same fragments (Figs. 10a, b) as distinct from A0080. In contrast, the CHNO compounds were differently distributed for the same alkyl homologues as observed in A0080 (Figs. 10c, d).

By FE-SEM–EDS observation, chondrule and anhydrous minerals were not found in the Orgueil, and secondary minerals such as magnetite, Fe–sulfide, Ca–sulfate, and Ca–phosphate (apatite) grains were abundant in the matrix of the Orgueil meteorite. The SOM was concentrated on the sample surface, mainly in three areas at ~100–200  $\mu\text{m}$  (Fig. 11). The maximum height difference observed on the sample surface was 80  $\mu\text{m}$ , which occurred in the DESI-HRMS analysis due to fragility similar to A0080 and the unevenness difference within the SOM concentration was less than about 10  $\mu\text{m}$ . There is no clear correlation between the height of the sample surface and the SOM distribution and (Additional file 1: Fig. S5). The CHO compounds-rich region tends to be enriched in CHN, CHNO, and CHO–Na as well,

while CHNO and CHO–Na compounds-rich region (~100  $\mu\text{m}$ ) was also observed (Fig. 11d). In the SOM-concentrated regions, large Ca–phosphate (10–20  $\mu\text{m}$ ), Fe–sulfide, and Mg–sulfate were distributed, but these minerals are also present in areas where SOM is not detected; thus, it was difficult to find a clear correlation between the distribution of minerals including secondary minerals and the spatial distribution of SOM.

For both fragments of Murchison, the identified SOM species were distributed in the matrix, where few chondrules and cracks were present (Figs. 12a–d). Fe–sulfide, magnetite, and Ca–sulfate occurred in both fragments, and large (> ~10  $\mu\text{m}$ ) carbonate grains were more abundant in fragment 1 than fragment 2 (Figs. 12c, e–f). The carbonate grains were Ca–carbonate, sometimes partially containing sodium, and appeared randomly distributed in the matrix of fragment 1. The difference of roughness of sample surface was less than about 50  $\mu\text{m}$ , and the SOM was widely distributed in the matrix in the sample, with no correlation with height similar to a previous study of DESI-HRMS analysis for a Murchison meteorite (Hashiguchi and Naraoka 2019b). The CHO, CHO–Na, and CHNO compounds seemed to be more concentrated in large (> 20  $\mu\text{m}$ ) Fe–sulfide-poor regions in fragment 1 (upper right region) than CHN compounds (Figs. 10c, d). However, these compounds were also detected from the surrounding of Fe–sulfide-rich region (the center region of fragment 1). The spatial distribution of SOMs seemed to be uncorrelated with specific minerals in each fragment, consistent with our previous work (Naraoka and Hashiguchi 2018). The intensity ratios of alkyl homologues of CHN and CHNO between fragment 1 (carbonate-rich) and fragment 2 (carbonate-poor) are compared in Fig. 13. The intensity ratios of alkyl CHN homologues in fragment 1 to fragment 2 increased with the of alkyl

**Table 2** Alkylated homologues of CHN, CHO, CHNO and CHONa compounds identified by DESI-HRMS imaging

	Formula	A0080	Orgueil	Murchison (fragment 1)	Murchison (fragment 2)
CHN	$C_nH_{2n+2}N^+$	<i>n.d.</i>	<i>n.d.</i>	9–16	9–16
	$C_nH_{2n}N^+$	<i>n.d.</i>	<i>n.d.</i>	10–11, 13–19	10–11, 13–19
	$C_nH_{2n-2}N^+$	<i>n.d.</i>	<i>n.d.</i>	14–18	14–18
	$C_nH_{2n-4}N^+$	14–15	17	12–21	12–21
	$C_nH_{2n-6}N^+$	14–15	<i>n.d.</i>	14–26	14–26
	$C_nH_{2n-8}N^+$	14–22	<i>n.d.</i>	15–27	15–26
	$C_nH_{2n-10}N^+$	15–21	<i>n.d.</i>	16–26	16–26
	$C_nH_{2n-12}N^+$	17–19	<i>n.d.</i>	17	17
	$C_nH_{2n-14}N^+$	17–20	<i>n.d.</i>	13	13
	$C_nH_{2n+3}N_2^+$	<i>n.d.</i>	<i>n.d.</i>	5	5
	$C_nH_{2n+1}N_2^+$	<i>n.d.</i>	<i>n.d.</i>	10–17	10–17
	$C_nH_{2n-1}N_2^+$	4	4	6–20	6–20
	$C_nH_{2n-3}N_2^+$	<i>n.d.</i>	<i>n.d.</i>	10–21	10–21
	$C_nH_{2n-5}N_2^+$	<i>n.d.</i>	<i>n.d.</i>	13–22	13–22
	$C_nH_{2n-7}N_2^+$	8	<i>n.d.</i>	11–21	11–21
	$C_nH_{2n-9}N_2^+$	15–17	<i>n.d.</i>	14–17	14–17
CHO	$C_nH_{2n+1}O^+$	<i>n.d.</i>	3–4, 7–8	8	8
	$C_nH_{2n-3}O^+$	<i>n.d.</i>	8–10	<i>n.d.</i>	<i>n.d.</i>
	$C_nH_{2n-5}O^+$	<i>n.d.</i>	7, 10	<i>n.d.</i>	<i>n.d.</i>
	$C_nH_{2n+1}O_2^+$	<i>n.d.</i>	5–7	8	8
	$C_nH_{2n-1}O_2^+$	<i>n.d.</i>	5, 7–10, 12	6	<i>n.d.</i>
	$C_nH_{2n-3}O_2^+$	<i>n.d.</i>	9, 10	<i>n.d.</i>	<i>n.d.</i>
	$C_nH_{2n+3}O_3^+$	<i>n.d.</i>	5–7, 10	<i>n.d.</i>	<i>n.d.</i>
	$C_nH_{2n-11}O_3^+$	<i>n.d.</i>	9	8, 10	8, 10
	$C_nH_{2n-8}O_4^+$	13–14	<i>n.d.</i>	8	8
	$C_nH_{2n-6}O_4^+$	9–16	<i>n.d.</i>	7	7
	$C_nH_{2n-4}O_4^+$	6–7, 10–16	<i>n.d.</i>	<i>n.d.</i>	<i>n.d.</i>
	$C_nH_{2n-2}O_4^+$	4–16	<i>n.d.</i>	<i>n.d.</i>	<i>n.d.</i>
	$C_nH_{2n}O_4^+$	5–15	<i>n.d.</i>	7	7
	$C_nH_{2n+2}O_4^+$	6–14	5	9	9
	$C_nH_{2n+2}O_5^+$	6, 9	<i>n.d.</i>	13	13
	$C_nH_{2n}O_5^+$	5, 9–11, 13	<i>n.d.</i>	8, 11	8, 11
$C_nH_{2n-2}O_5^+$	9–13	<i>n.d.</i>	9	9	
$C_nH_{2n-4}O_5^+$	9–12, 14–15	<i>n.d.</i>	<i>n.d.</i>	<i>n.d.</i>	
$C_nH_{2n-6}O_5^+$	11, 13	<i>n.d.</i>	<i>n.d.</i>	<i>n.d.</i>	
CHNO	$C_nH_{2n}ON^+$	<i>n.d.</i>	<i>n.d.</i>	11, 14	11, 14
	$C_nH_{2n-2}ON^+$	6, 8, 11–14	<i>n.d.</i>	<i>n.d.</i>	<i>n.d.</i>
	$C_nH_{2n-4}ON^+$	6, 8, 12–15	<i>n.d.</i>	8, 10–19	8, 10–19
	$C_nH_{2n-6}ON^+$	<i>n.d.</i>	<i>n.d.</i>	12–19	12–19
	$C_nH_{2n-8}ON^+$	<i>n.d.</i>	<i>n.d.</i>	16–21	16–21
	$C_nH_{2n-1}ON_2^+$	<i>n.d.</i>	<i>n.d.</i>	8, 10–11, 14–18	8, 10–11, 14–18
CHONa	$C_nH_{2n-3}ON_2^+$	<i>n.d.</i>	<i>n.d.</i>	15, 16	15, 16
	$C_nH_{2n-2}O_6N^+$	<i>n.d.</i>	<i>n.d.</i>	18, 22	18, 22
	$C_nH_{2n-4}ONa^+$	8, 11–12, 14	<i>n.d.</i>	<i>n.d.</i>	<i>n.d.</i>
	$C_nH_{2n-4}ONa^+$	8, 9, 11, 14, 16	<i>n.d.</i>	<i>n.d.</i>	<i>n.d.</i>
	$C_nH_{2n-8}ONa^+$	8, 12–14	<i>n.d.</i>	<i>n.d.</i>	<i>n.d.</i>
	$C_nH_{2n}O_3Na^+$	<i>n.d.</i>	8, 9, 12	<i>n.d.</i>	<i>n.d.</i>
$C_nH_{2n+2}O_3Na^+$	<i>n.d.</i>	4, 5, 7, 10	4, 6	4, 6	



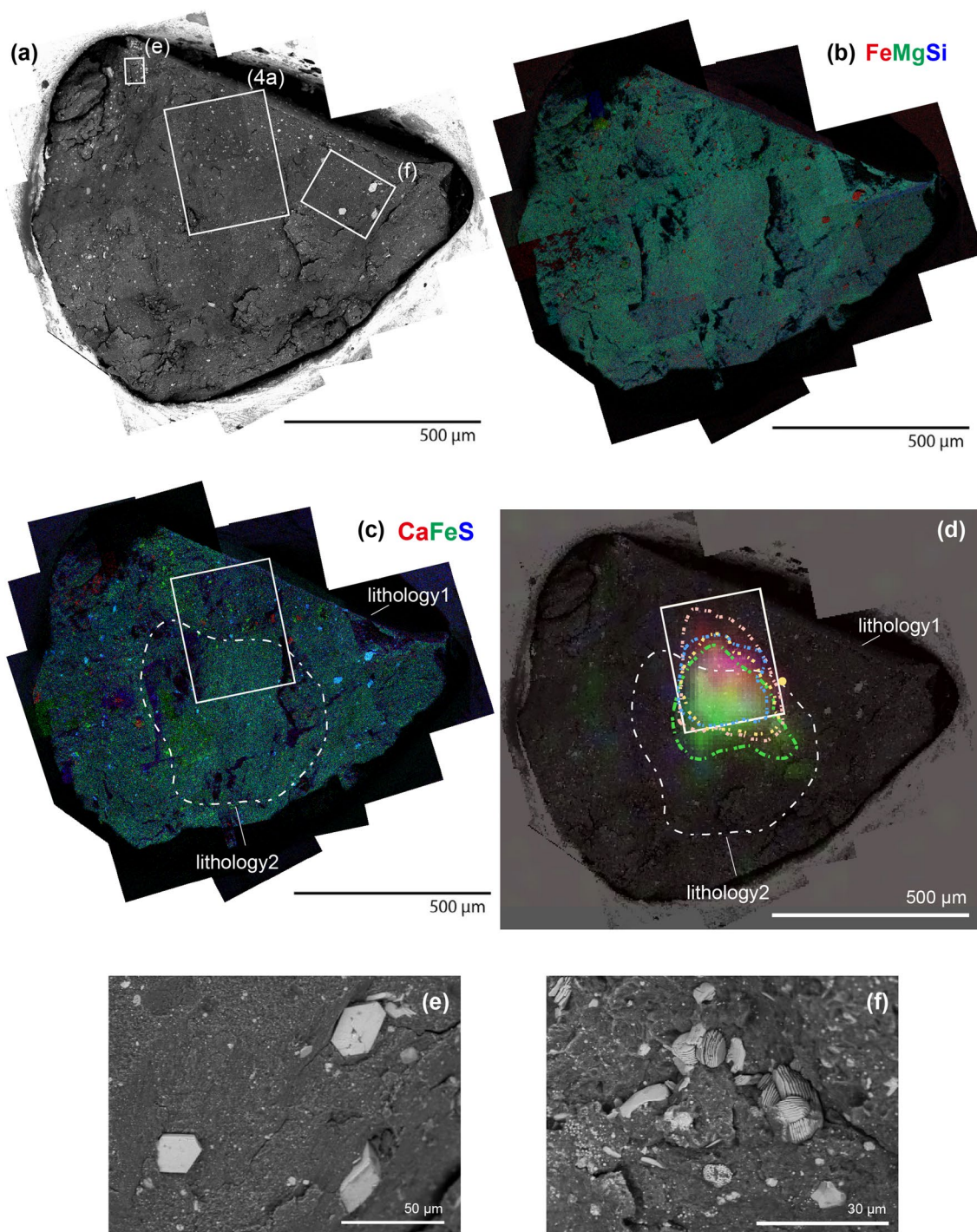


**Fig. 3** **a** BSE image of A0080. **b** RGB maps corresponding to Fe-K $\alpha$  (red), Mg-K $\alpha$  (green), and Si-K $\alpha$  (blue). In this image, anhydrous silicates and chondrules would be shown in bright green. **c** RGB maps of Ca-K $\alpha$  (red), Fe-K $\alpha$  (green), and S-K $\alpha$  (Blue). Bright blue grains and bright green grains correspond to Fe-sulfide (pyrrhotite) and magnetite, respectively. Red grains show Ca- and Ca-Mg carbonate (dolomite). A dotted outline shows boundary lithology 1 (outside), which contains abundant magnetite, pyrrhotite, and dolomite, and lithology 2 (inside). **d** A combined image of the BSE image with overlaid RGB images of total CHO (Red), CHN (Green) and CHNO (Blue), which are the same figure shown in Fig. 2b. Dotted lines show outlines of the concentrated region for total CHO (pink), total CHN (green), total CHNO (blue), and total CHO-Na (yellow), which is almost consistent with total CHNO, respectively. Note that positioning of the DESI-HRMS images to BSE image contains an uncertainty of  $\pm \sim 20 \mu\text{m}$ . **e, f** pyrrhotite and magnetite grains with various crystal shapes, which were obtained from area **(e)** and **(f)** shown in **(a)**

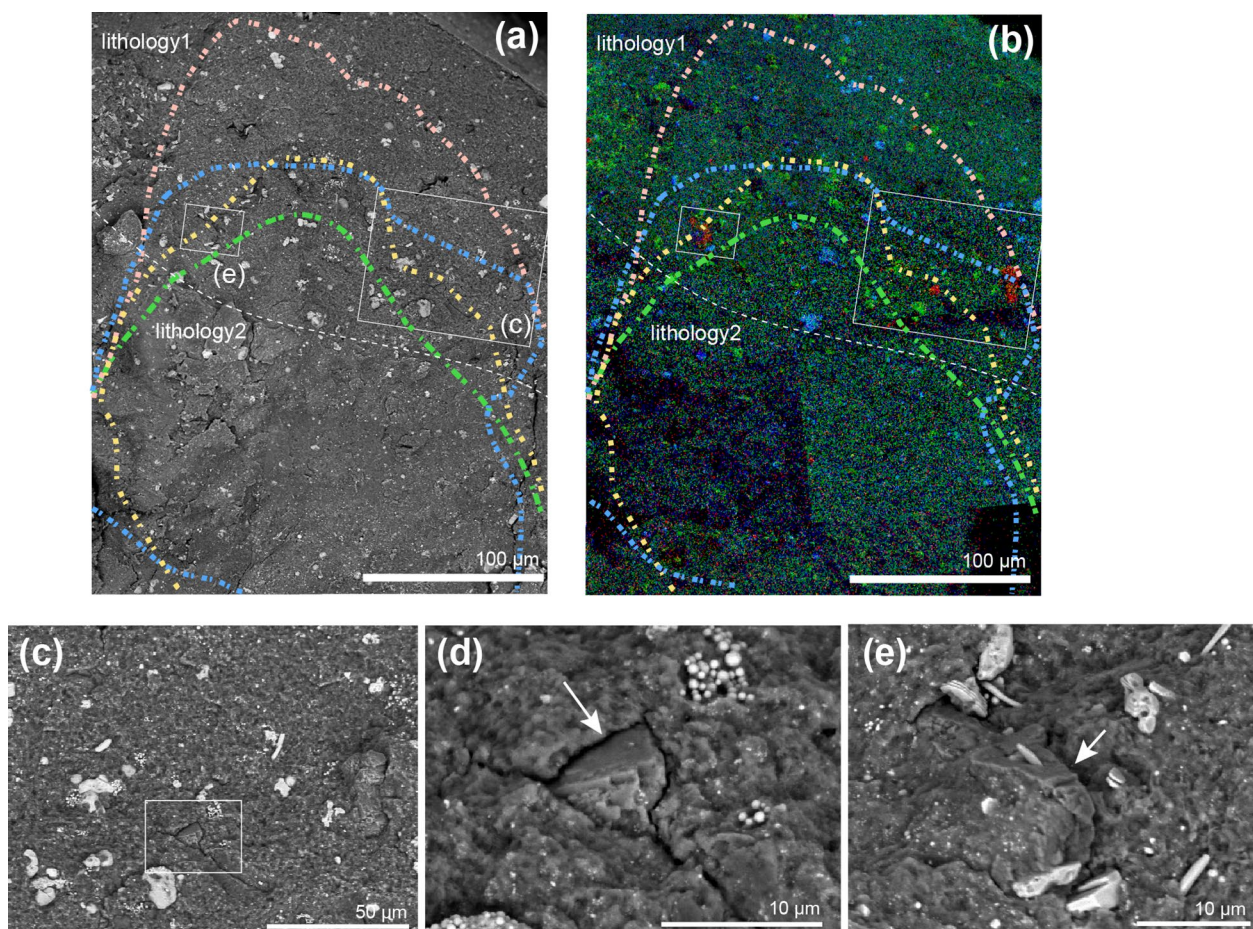


**Fig. 4** **a** High magnification BSE image and **b** RGB maps of Ca–K $\alpha$  (red), Fe–K $\alpha$  (green), and S–K $\alpha$  (Blue), which are obtained from the same area shown as **(a)** in Fig. 3a. The dotted lines and the color are the same as that shown in Fig. 3b. The upper region in this area (lithology 1) contains a lot of magnetite, pyrrhotite, and Ca–Mg carbonate (dolomite) of > 10  $\mu$ m size. In the lower region, such large secondary minerals were less abundant (lithology 2). **c** High-magnification BSE image obtained from the area **(c)** shown in **(a)**. **d**, **e** BSE image of dolomite grains, which corresponds to the same area shown as a square in **(c)**, as **(e)** and Fig. 4a, respectively

size of CHN homologues for  $C_nH_mN^+$  (Fig. 13b). On the other hand,  $C_nH_mN_2^+$  compounds showed a similar intensity ratio between fragment 1 and fragment 2. The relationship of alkyl homolog size of CHN compounds and distribution of carbonate in the two Murchison fragments is distinct from that observed in A0080. No clear correlation was found amongst CHNO compounds (Fig. 13c).

## Discussion

### Molecular diversity of identified SOMs in A0080

DESI-HRMS imaging revealed a variety of methanol-soluble organic compounds on the surface of A0080, because DESI technique is related to solubility of spray solvent (e.g., Ifa et al. 2007). The molecular diversity and distribution patterns of organic compounds with various soluble organic compounds including aliphatic amines, carboxylic acids, polycyclic aromatic

hydrocarbons, amino acids, and alkylated N-bearing heterocyclic compounds were previously reported from the solvent extracts of Ryugu aggregate sample A0106 (Naraoka et al. 2023). Alkylated homologues of N-heterocycles having a core structure with additional methylene such as piperidine ( $C_nH_{2n+2}N^+$ ), pyridine ( $C_nH_{2n-4}N^+$ ), and imidazole ( $C_nH_{2n-1}N_2^+$ ) were identified in the methanol extract of the A0106 (Naraoka et al. 2023). Such N-heterocycles were also reported previously from the extracts of the Murchison meteorite (Naraoka et al. 2017). Although there are differences in ionization efficiency due to the analytical methods described here, the identification of the alkylated CHN compounds from A0080 and Murchison by DESI-HRMS in this study is consistent with the detection of those compounds in the solvent extracts.

On the other hand, those alkylated CHN compounds were not identified in the Orgueil meteorite. The result

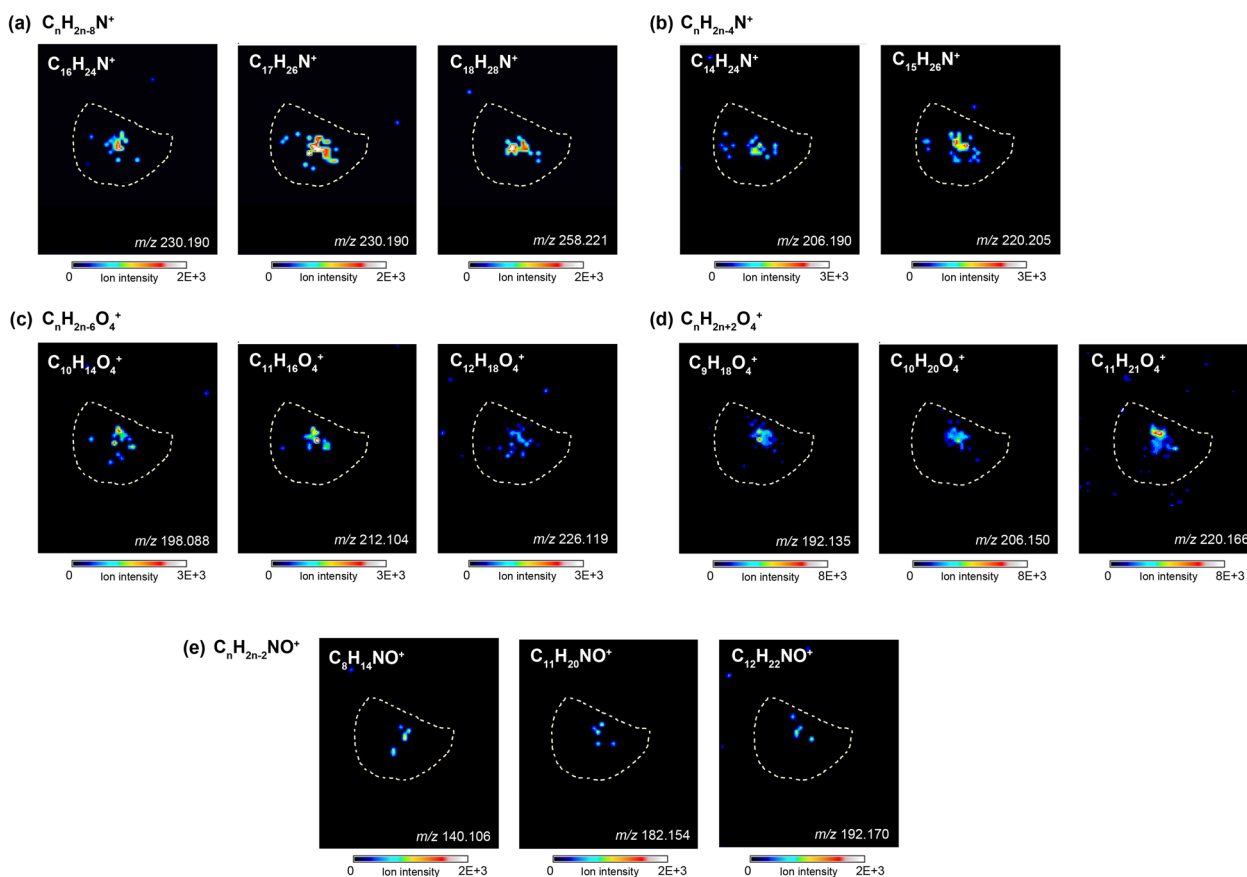


**Fig. 5** Representative ion intensity images of alkylated homologues of **a**  $C_nH_{2n-6}N^+$ , **b**  $C_nH_{2n-4}N^+$ , **c**  $C_nH_{2n-6}O_4^+$ , **d**  $C_nH_{2n+2}O_4^+$  and **e**  $C_nH_{2n-2}NO^+$ , identified from A0080 respectively

suggests the different mechanism to produce and evolve the CHN compounds between in Orgueil and in Ryugu including fluid composition on their parent body despite of their similar feature such as mineralogy, elemental and isotopic composition. Effect of space weathering or perhaps terrestrial alteration are also possible mechanisms to produce different abundance of CHN compounds in Orgueil and A0080 that described later. A Ryugu grain A0080 and Orgueil were dominated by CHO compounds or CHO–Na compounds, on the other hand, Murchison meteorites were rich in CHN and CHNO compounds (Figs. 2a, 8c; Table 1).

More abundant alkyl homologues of CHN compounds such as the  $C_nH_{2n-4}N^+$  composition with a wider range of alkylation sizes were identified in Murchison than in A0080 (Table 2). In contrast to the present result in this study for A0080, the distribution pattern of alkylpyridine ( $C_nH_{2n-4}N^+$ ) identified from methanol extract of A0106 showed a wider C range relative to Murchison, suggesting different hydrothermal activity and/or different history of solar radiation and cosmic ray irradiation between Ryugu and the parent

body of the Murchison meteorite (Naraoka et al. 2023). The difference of molecular diversity of A0080 found in this study was not consistent with data of A0106 completely, and that result would be attributed to difference of analytical technique using (Nano-) ESI and DESI ionization effect. For example, imidazole and hydroxy pyridine show high sensitivity as positive ions ( $[M+H]^+$ ) by both ESI and DESI in flow or spray of solvent. On the other hand,  $[M+H]^+$  ions of pyridine, crown ether, glycine, and phthalaldehyde showed low ionization and desorption efficiency although they showed high sensitivity in ESI analysis (Additional file 1: Fig. S6, Table S1). Furthermore, considering the heterogeneous spatial distribution of SOM observed in this study, the difference might also be the result of sample heterogeneity—in other words, heterogeneity of SOM distribution in the CC (Naraoka and Hashiguchi 2018; Hashiguchi and Naraoka 2019b; this study) and in the Ryugu sample. Based on our supplementary data (Additional file 1: Fig. S6, Table S1), pyridines (and possibly alkylpyridines) detected by DESI-HRHS in this study

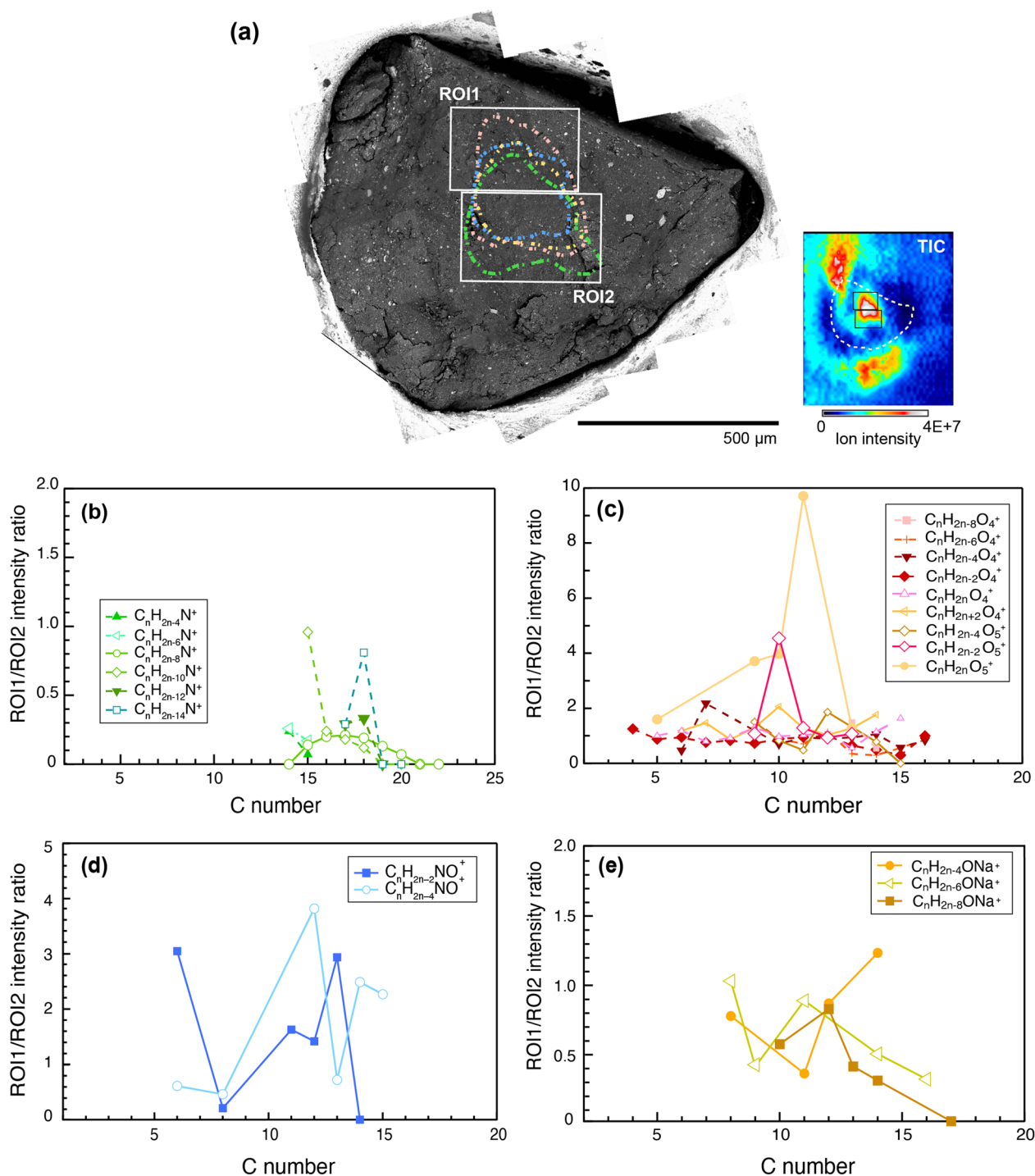


**Fig. 6** a BSE images of A0080 with ROI1 and ROI2, almost corresponding to lithology 1 and lithology 2. Total intensity ratio between ROI1 and ROI2 as a function of size of alkylated homologues of **b** CHN compounds, **c** CHO compounds, **d** CHNO compounds, and **e** CHO–Na compounds, respectively

would be underestimated in abundance compared to (alkyl-)imidazoles estimated from their ion intensities.

The differences between the Murchison and Orgueil meteorites would result from differences in the organic matter accreted in their parent bodies or formation

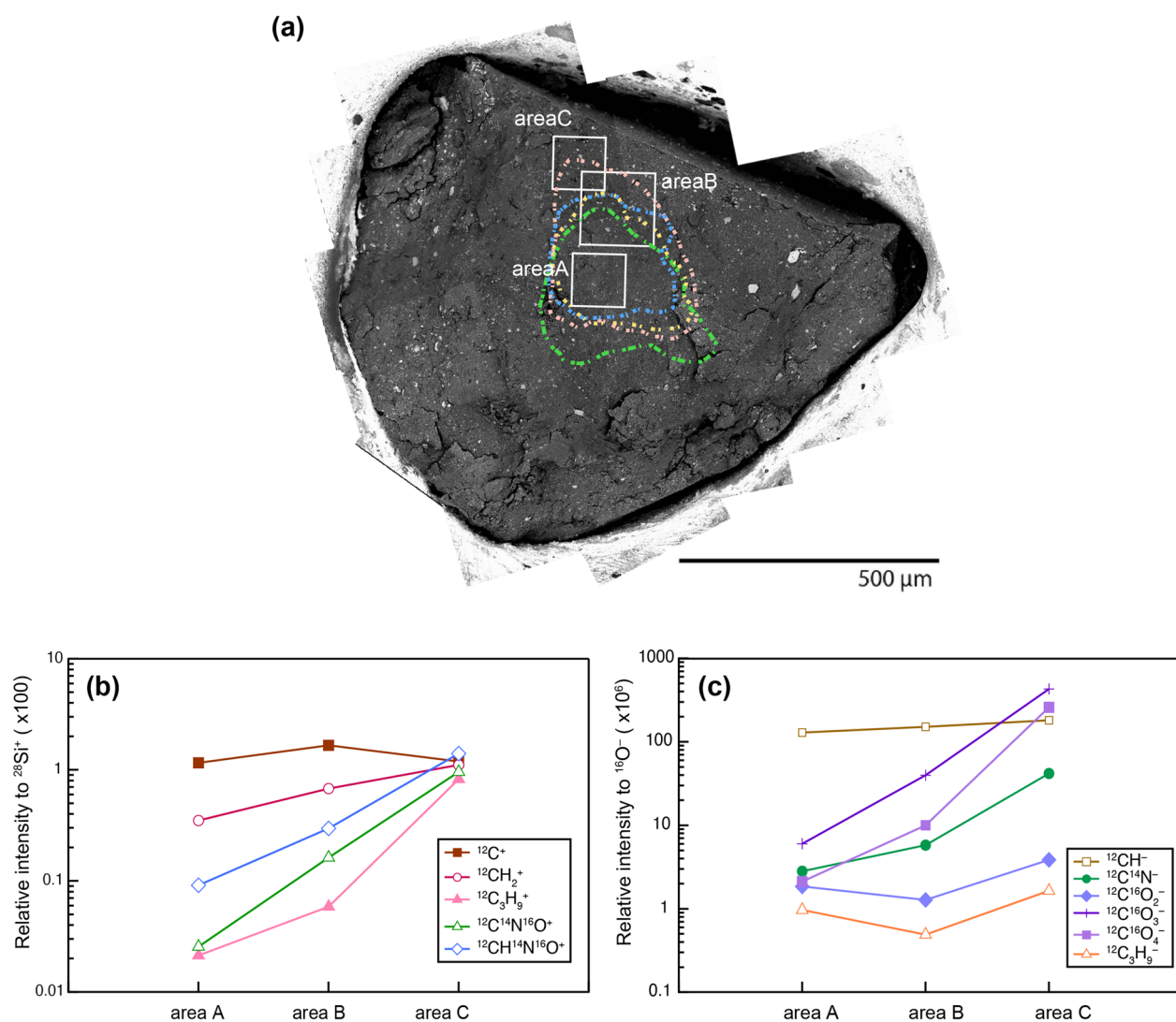


**Fig. 7** **a** BSE image of A0080. White squares show the analyzed area by TOF–SIMS. Dotted lines are corresponding to outlines for concentrated regions of CHO (pink), CHNO (blue), CHN (green), and CHO–Na (yellow) compounds, respectively. **b** Ion intensity of  $^{12}\text{C}^+$ ,  $^{12}\text{CH}_2^+$ ,  $\text{C}_3\text{H}_9^+$ ,  $\text{CNO}^+$ , and  $\text{CHNO}^+$  ions relative to  $^{28}\text{Si}^+$  ions. **c** Relative intensity of  $\text{CH}^-$ ,  $\text{CN}^-$ ,  $\text{CO}_2^-$ ,  $\text{CO}_3^-$ ,  $\text{CO}_4^-$ , and  $\text{C}_3\text{H}_9^-$  ions to  $^{16}\text{O}^-$  from area A, area B and area C, shown in (a) respectively

process of SOM, and subsequent alteration conditions on the parent bodies. In particular, the alkyl homologues of CHN are thought to have formed and grown as a result of fluid activity during the aqueous alteration (Naraoka et al. 2017), therefore differences in fluid composition and the aqueous alteration environment may be responsible for the differences.

The effect of space weathering needs to be considered for the result from Ryugu grain A0080 because it could have experienced space weathering due to solar wind sputtering and micrometeorite bombardment (Noguchi et al. 2022), and also solar heating. Destruction of the chemical bonds of SOM could have occurred by UV

irradiation, which may result in the loss of  $\text{H}_2$ , methane, water, or aliphatic features (Orthous-Daunay et al. 2019). UV irradiation has also been argued as important mechanism for degradation of several organic molecules and biosignatures on Mars (Carrier et al. 2019). The penetration depth of UV irradiation on Ryugu has not been accurately estimated so far. Although the accurate estimate is difficult due to difficulty of obtaining standard mineral samples with UV transparent, it would be a few to several hundred nm order based on the investigations with various natural minerals (Carrier et al. 2019) and the penetration depth of solar wind injection in Ryugu grains ( $\sim 100$  nm; Noguchi et al. 2022). Under the analytical

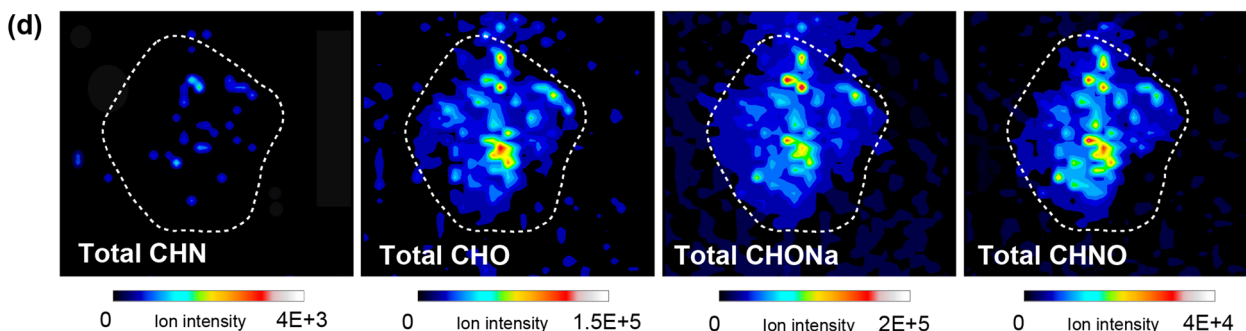
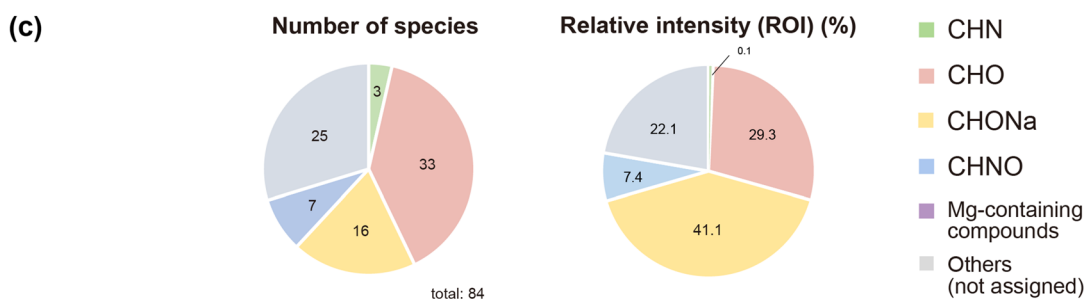
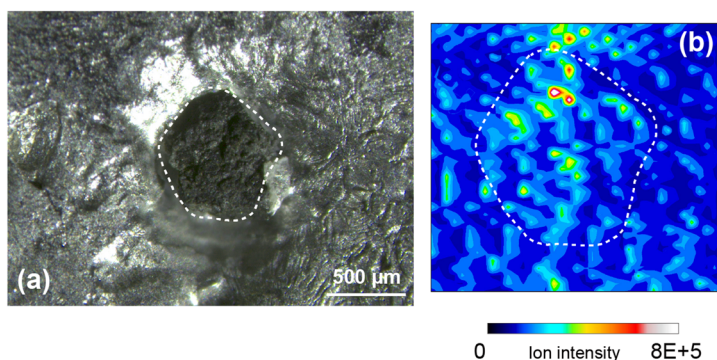


**Fig. 8** **a** An optical microscope image of the Orgueil meteorite. The dotted line represents the boundary of the meteorite grain and the surrounding soft alloy. **b** A total ion image obtained by DESI-HRMS. **c** The number of species and the relative intensity (%) of identified from Orgueil. The relative intensity was calculated using total intensity from ROI (inside of the dotted line in (a), (b)). **d** DESI-HRMS images of total ions of CHN, CHO, CHO–Na, and CHNO compounds, respectively

conditions of DESI-HRMS used in this study, the penetration depth on the surface of the sample is about ~200–500 nm. Because this estimate is based on Rhodamine B with high solubility and permeability for methanol solvent, the penetration depth may be shallower for Ryugu or meteorite samples depending on porosity in the sample.

Based on those, UV irradiation would have affected on the SOM in the surface of A0080 that was identified by DESI-HRMS and generated from a sample surface of less than 500 nm. On the other hand, molecular analysis of organic matter of Orgueil and Murchison meteorites was performed on interior material that should not have been significantly affected by space weathering rather than surface material of Ryugu. Hence, space

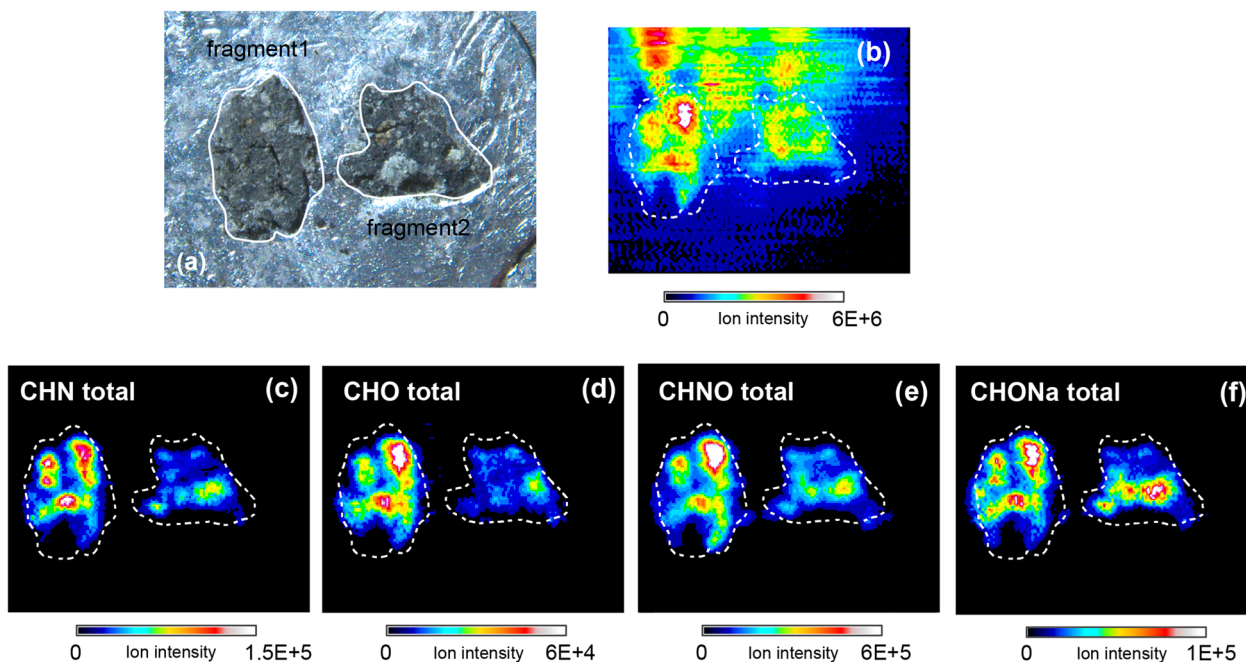


**Fig. 9** **a** Optical microscope image of Murchison fragments embedded in Indium. **b** TIC image of DESI-HRMS imaging. Total ion intensity image for **c** CHN compounds, **d** CHO compounds, **e** CHNO compounds, and **f** CHO–Na compounds. Dotted lines in **b–f** show outlines of the sample surface of fragment 1 and fragment 2

weathering is a possible explanation for the difference in molecular diversity of A0080 compared to the Orgueil and Murchison meteorites. A comparison of these results with those from the second sample collected

by Hayabusa2, which is composed of material, more likely to have derived from Ryugu’s subsurface would be illuminating.

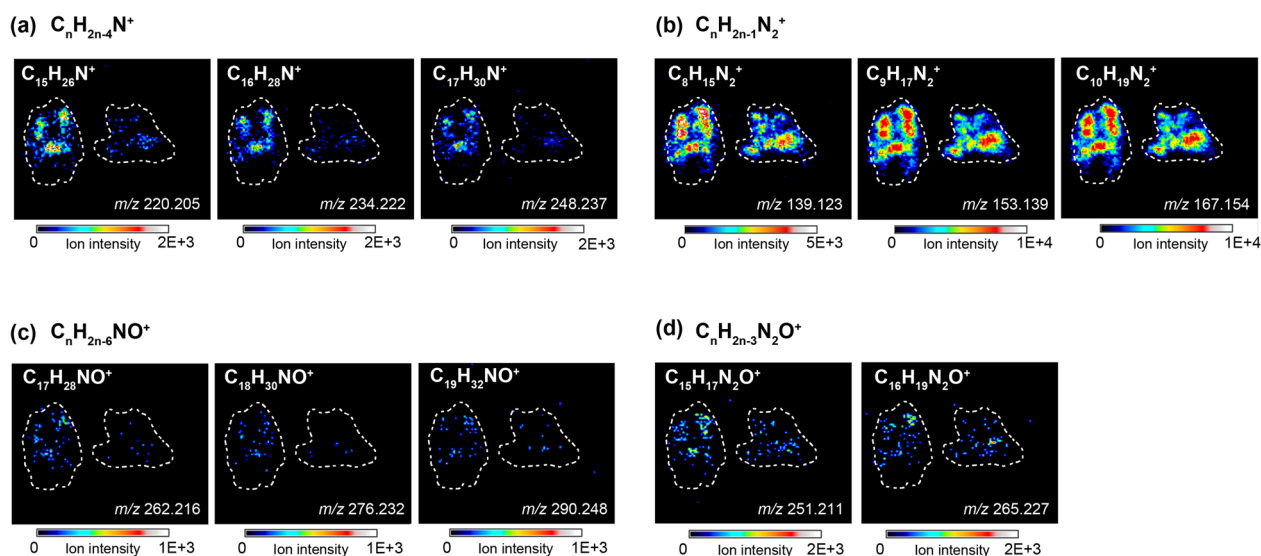


**Fig. 10** Representative ion intensity images of alkylated homologues of **a**  $C_nH_{2n-4}N^+$ , **b**  $C_nH_{2n-1}N_2^+$ , **c**  $C_nH_{2n-6}NO^+$ , and **d**  $C_nH_{2n-3}N_2O^+$  from Murchison fragments

### Spatial distribution of SOM in A0080 and implication for interaction with minerals or aqueous fluid

The organic compounds identified in A0080, Orgueil, and Murchison by DESI-HRMS imaging in this study are methanol-soluble. The Ryugu samples experienced by aqueous alteration (Nakamura et al. 2022; Yokoyama et al. 2022), and the identified organic compounds, should have been dissolved in the aqueous fluid. The FE-SEM-EDS observations revealed that large ( $>10\ \mu\text{m}$ ) sulfide, magnetite, carbonate grains were heterogeneously distributed in A0080, as seen in lithology 1 and 2. These minerals, particularly magnetite and carbonate, were produced during aqueous alteration (Brearley et al. 2006) and SOM distributions appear to be related to the mineral distribution (more concentrated in lithology 1 or lithology 2, as discussed above). Therefore, the different spatial distributions of the SOMs (CHN, CHO, CHO–Na, and CHNO; Fig. 2) are likely to be products of the aqueous activity in Ryugu's parent body, for example, interaction of minerals and fluids that contain SOMs. Mineral precipitation and compound adsorption with surrounding minerals is one of the key processes for different compound distribution. There are three possible mechanisms for producing the SOM heterogeneities. These are (a) presence of multiple fluids with different chemical compositions (abundance of CHN, CHO, CHO–Na, and CHNO) during aqueous alteration, which can be ascribed to the different chemical compositions of interstellar ice grains accreted to the parent body, and distribution of each fluid to different range of the body, (b) different timing of SOM precipitation, and (c) different transportation efficiency of organic compounds by fluid flow and adsorption effect onto surrounding minerals. These will be considered individually below. (a) A variety of chemical compositions in initial ice grains is not implausible based on chemical compositions of cometary ice (Goesmann et al. 2015; Bockelée-Morvan and Biver 2017) and numerous laboratory studies (e.g., Piani et al. 2017). Also, ice grains with various chemical compositions should have been present based on the stability of molecules with heliocentric distance and changes in condition on the solar nebula (e.g., Dodson-Robinson et al. 2009). Although there has been no evidence found in the Ryugu sample that traces accumulation of ice particles with different elemental and isotopic compositions as have been observed in the Isheyevo meteorite (CH chondrite) (van Kooten et al. 2017), previous studies suggest that asteroid Ryugu originated from the outer solar system (Hopp et al. 2022; Ito et al. 2022; Kawasaki et al. 2022). Based on the various organic compositions of cometary ice, it is possible that ice particles of various

compositions may have accumulated on the Ryugu parent body.

In this study, CHO, CHN, CHO–Na, and CHNO compounds were identified in a small region of a few hundred  $\mu\text{m}$  and more than half of the region for these SOMs overlapped. The concentrated region of CHO, CHN, CHNO, and CHO–Na compounds gradually changed and appeared to be the result of fluid transportation. Bland et al. (2009) showed that the permeability of CC parent bodies, which are composed mainly of nanoscale particles (grain size in the range 20–200 nm), is low, and the maximum distance that fluid can be transported during an aqueous alteration of about 1 Ma is up to 100 s of  $\mu\text{m}$  (Bland et al. 2009). If nanoscale ice grains of various chemical compositions were heterogeneously distributed on the Ryugu parent body and they melt and fluid is consumed in situ, the spatial distribution of SOM would likely to be a more heterogeneous than if the fluid was gradually displaced, as we observed. Furthermore, it is not necessary for a correlation with the mineral and SOM distribution if the SOM distribution simply reflects the composition and location of the ice grains accreted in the Ryugu parent body. Therefore, (a) is unlikely to produce the different distribution of SOM. (b) Organic ions from ice grains and cations (e.g.,  $\text{Mg}^{2+}$ ,  $\text{Fe}^{2+}/\text{Fe}^{3+}$ , and  $\text{Ca}^{2+}$ ) were generated by dissolution of anhydrous or amorphous silicates during aqueous alteration (Brearley 1995; Howard et al. 2009) on the asteroid Ryugu parent body. These organic ions in fluids would have been precipitated as salts in secondary minerals, such as carbonate and phosphate, as the aqueous fluid was consumed by the alteration process (Le Guillou et al. 2014). Nanoscale observations of CCs including Orgueil suggests that nanocarbonate co-precipitated with organic matter during aqueous alteration on the parent body (Le Guillou et al. 2014). Further, organo-carbonates were observed in CCs (Chan et al. 2017); therefore, it follows that SOM is closely related to mineral formation and precipitation in fluids.

The CHO compounds in A0080 were more abundant in lithology 1 than other SOMs. Carboxylic acids are mainly ionized as negative ions by electrospray ionization (ESI), not detected as positive ion (Thurman et al. 2001) (Additional file 1: Table S1). Although the chemical structures are not available for this analysis, the ionization and desorption efficiencies of DESI suggest that these CHO compounds may be ethers or aldehydes (especially those with aromatic rings) (Additional file 1: Fig. S6, Table S1). The influence of the formation and growth of carbonates on organic matter has been investigated in previous experimental studies, for example focused on carboxylic acids (Wada et al. 1999, 2001; Roberts et al. 2013) or alcohols (Dickinson and McGrath 2003). Effect of aldehydes and



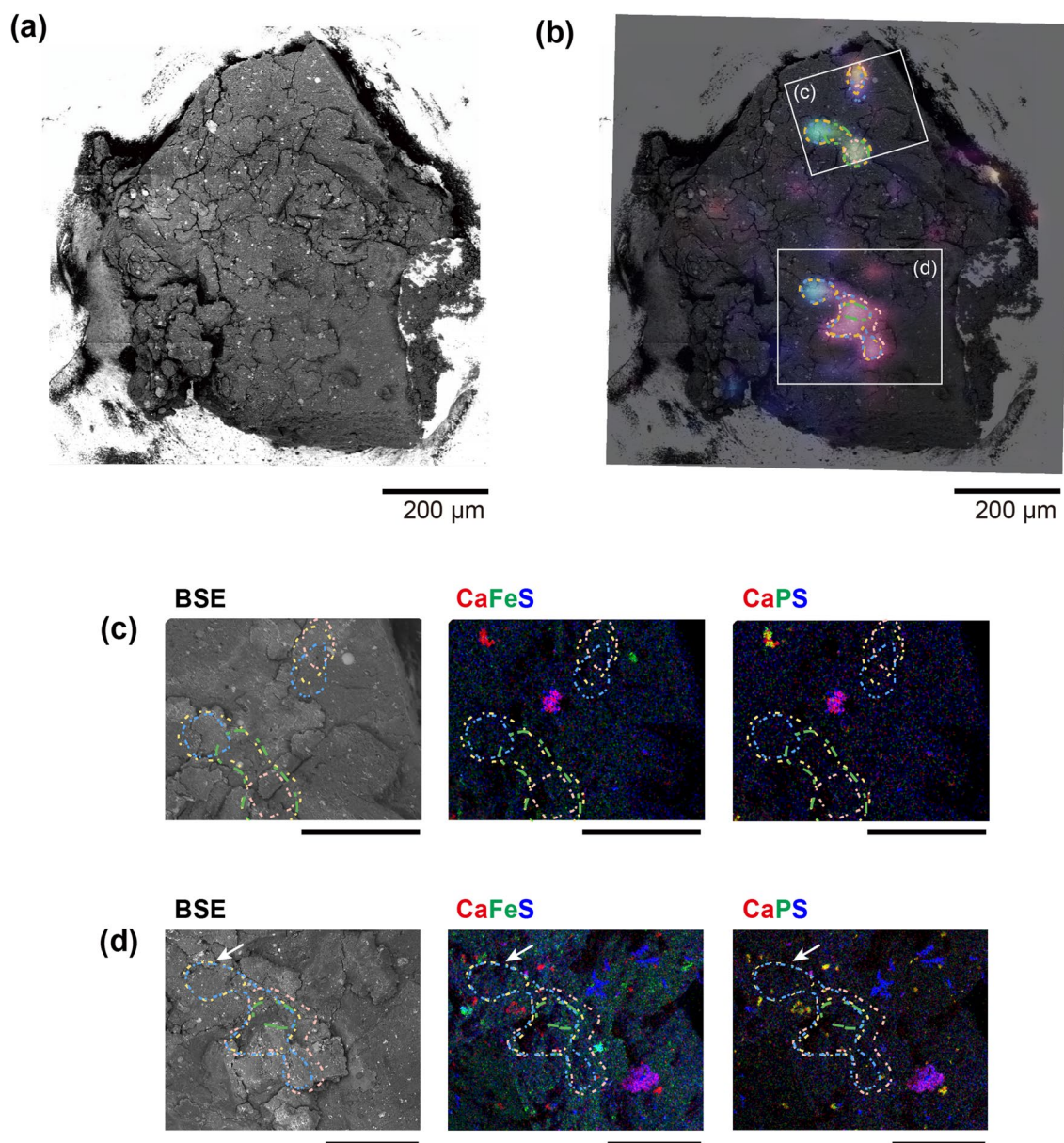


**Fig. 11** **a** BSE image of the Orgueil meteorite. **b** A combined image of the BSE image with overlaid RGB images of total CHO (Red), CHN (Green) and CHNO (Blue). Dotted lines show outlines of the concentrated region for total CHO (pink), total CHN (green), total CHNO (blue), and total CHO–Na (yellow), respectively. Those outlines are corresponding to an ion intensity of  $>40\%$  of the maximum intensity for each compound. Note that positioning of the DESI-HRMS images to BSE image contains an uncertainty of  $\pm \sim 20 \mu\text{m}$ . **c**, **d** BSE and RGB maps of Ca (Red) Fe (Green) and S (Blue) or Ca (Red) P (Green) and S (Blue) of SOM concentrated regions shown in **(c)** and **(d)** in **(b)**. In RGB maps of Ca (Red) Fe (Green) and S (Blue), light green and purple grains are corresponding Fe–sulfide, which almost pyrrhotite, and Ca–sulfate, respectively. In region **(d)**, many Ca-phosphate (apatite) are observed by yellow color in RGB maps of Ca (Red) P (Green) and S (Blue). Large grains shown in blue color in both RGB maps (CaFeS and CaPS) are corresponding to Mg sulfate. All scale bars for images in **(c)** and **(d)** correspond to  $100 \mu\text{m}$

ethers for precipitation of carbonates have not been investigated in detail, but these compounds may have affected the carbonate formation reaction in the fluid, or they may have preferentially adsorbed and coprecipitated on carbonates in A0080 based on our observation.

In contrast to CHO compounds, CHN, CHNO, and CHO–Na compounds were more concentrated in lithology 2 than in lithology 1, though the distribution of these compounds mostly overlapped (Fig. 3d). As discussed above, these compound-enriched regions are gradually displaced, and it would appear to be the result of fluid

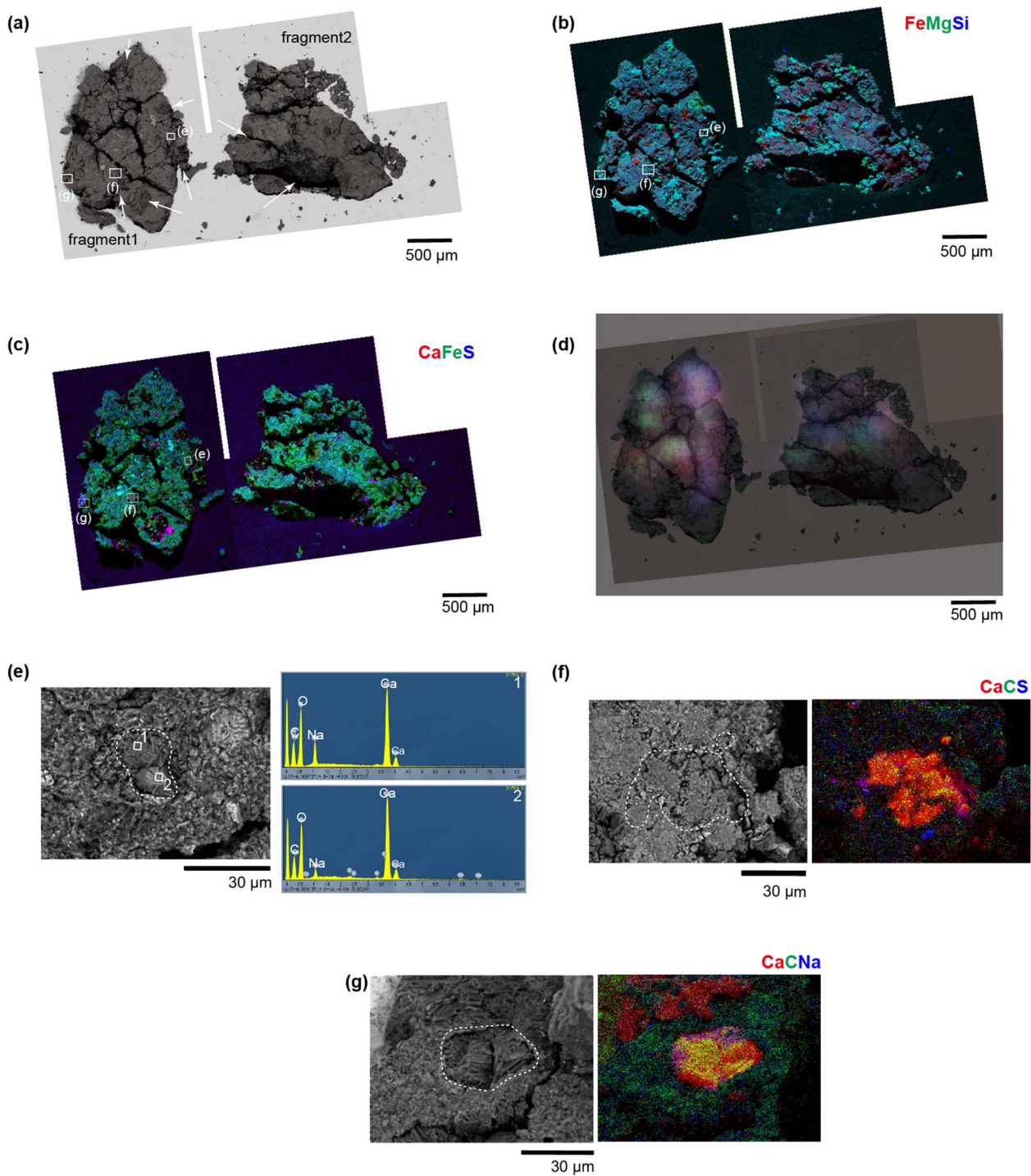


**Fig. 12** **a** Back-scattered image of Murchison fragments. White arrows show chondrules or their fragments. Black veins correspond to cracks. **b** Combined RGB map corresponding to Fe-Ka (red), Mg-Ka (green), and Si-Ka (blue). Red grains are Fe-sulfide or magnetite. **c** Combined RGB map of Ca-Ka (red), Fe-Ka (green), and S-Ka (blue). Pink grains and bright green grains correspond to Ca-sulfate, and Fe-sulfide, respectively. **d** A combined image of the BSE image with overlaid RGB images of total CHO (red), CHN (green), and CHNO (blue). **e** BSE image (left) and EDS spectra (right) obtained from area1 and 2 shown in the BSE image. The EDS spectra consist of Ca, Na, C, and O. **f** BSE image of carbonate grain and RGB map of Ca-Ka (red), C-Ka (green), and S-Ka (blue). The grain is mainly Ca-carbonate and partially contains sulfate. **g** BSE image of a Ca-Na carbonate grain and RGB map of Ca-Ka (red), C-Ka (green), and Na-Ka (blue). **(e)-(g)** correspond to the same area shown by squares in **(a)-(c)**

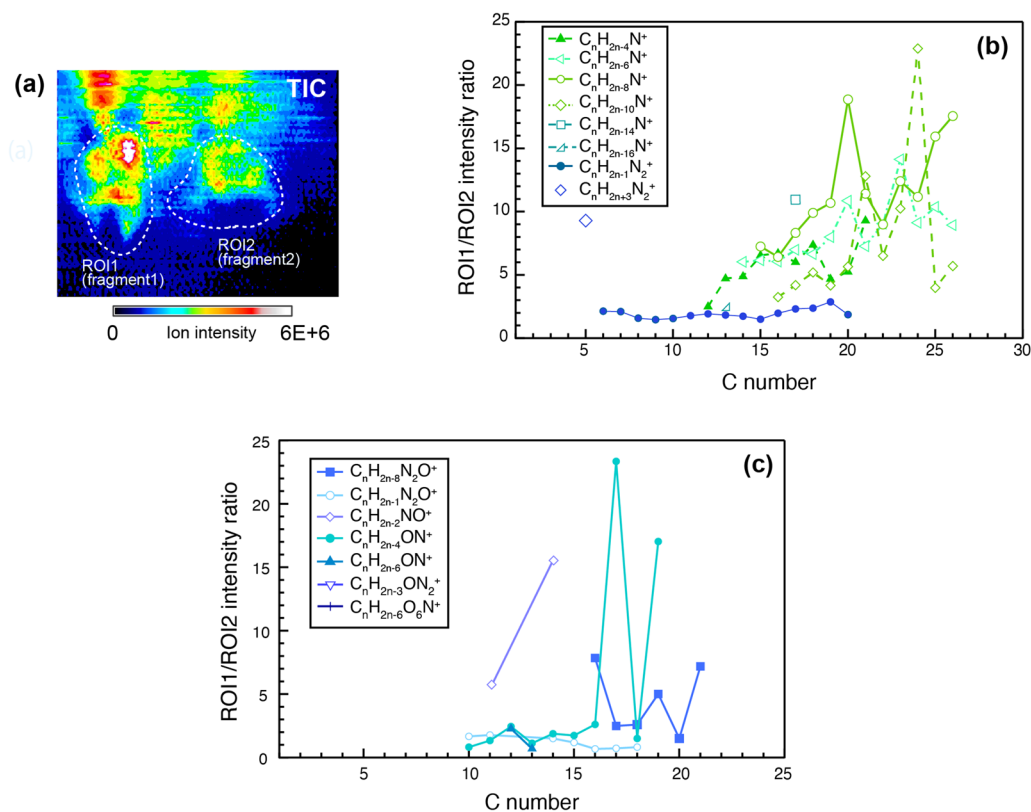


**Fig. 13** a TIC image of Murchison fragments with ROI1 and ROI2, almost corresponding to the whole sample surface of fragment 1 and fragment 2, respectively. Total intensity ratio from ROI1 to ROI2 as a function of size of alkylated homologues of **b** CHN compounds, and **c** CHNO compounds

migration. The distance between the CHO-rich region (upper region) and the CHN-rich region (lower region) is approximately 100  $\mu\text{m}$  (Fig. 3d). Ryugu, which has CI-like features, has undergone extensive aqueous alteration on its parent body. Similar alterations lasted 9 Ma on the CI parent body (Fujiya et al. 2013). Since it is possible that fluid is transported up to 100 s of  $\mu\text{m}$  during 1 Ma of aqueous alteration (Bland et al. 2009), it is plausible that this is the result of fluid transport observed in this study.

A possible scenario involved two steps. First, CHO compounds in the aqueous fluid catalyzed dolomite precipitation and some fraction of the CHO compounds precipitated in lithology 1 together with dolomite and  $Mg^{2+}$  ions to form dolomite grains. Subsequently, the fluid moved to lithology 2 and was gradually consumed. As a result, the remaining CHO compounds and CHN, CHO-Na, and CHNO compounds were also precipitated from the dwindling fluid. The CHO compounds showed high ion intensities in lithology 1, thus, abundant CHO compounds, which may include ethers and aldehydes, could have been precipitated during dolomite formation. Nano-scale investigation for the relationship of mineral surfaces to interiors would provide more constraint for the fluid actions. (c) The fluid activity could produce the

observed heterogeneous distribution of soluble organic compounds (Naraoka and Hashiguchi 2018; Hashiguchi and Naraoka 2019b; Potiszil et al. 2020; Muneishi and Naraoka 2021). The transportation efficiencies of SOMs by fluid flow vary with their affinities for the aqueous phase (Potiszil et al. 2020) and adsorption onto surrounding minerals such as phyllosilicates. This process is like chromatography between the aqueous phase (mobile phase) and minerals (solid phase) (asteroidal chromatography). Geochromatographic phenomena between clay minerals and/or solubility in  $H_2O$  to produce fractionation of N-heterocycles have been observed in terrestrial environments (Yamamoto 1992) and postulated to have occurred in the parent bodies of the CCs (e.g., Wing and Bada 1991).

The adsorption of organic compounds on minerals has been previously observed, especially on clay minerals such as phyllosilicates by ion exchange (Bolger 1983; Hashizume 2015; Awad et al. 2019), and also on carbonates (Thomas et al. 1993). Wada et al. (2001) reported the strong affinity of carboxylic acid for  $CaCO_3$ , which resulted in the inhibition of  $CaCO_3$  growth. If adsorption was the main process that caused the different spatial distributions of SOMs in A0080, clear relationships between

more specific minerals and organic compounds should be observed. However, different transportation rates between CHO, CHN, CHNO (CHO–Na) compounds are also possible (Muneishi and Naraoka 2021), adding complexity to the interpretation of the different spatial distribution of these SOM. Further investigation of the transportation mechanisms of CHO, CHN, CHNO compounds will be needed before it will be possible to make a firm interpretation.

Ryugu samples and Orgueil have similar chemical characteristics; however, they were not similar in relation to SOM spatial distribution and mineral distribution. In particular, the different compositions and abundances of the SOM detected for the CHN compounds raise the possibility that the organic species they contain are different. Ryugu shows different distributions and abundances of amino acids and amines compared to Orgueil, suggesting that the evolutionary processes in the parent body, such as formation environment, pathways, and during water alteration, were different (Naraoka et al. 2023). Although the possibility of differences of primary organic matter accreted in the parent bodies of Orgueil and Ryugu cannot be completely ruled out, different features of the relationship of SOM distribution and minerals between these two samples may be due to differences in the formation process of each organic material, especially the interaction behavior with minerals due to processes in the parent body.

Our results showed that the relationship between SOM and dolomite, which is a secondary mineral observed in A0080, suggests that the fluid activity is likely responsible for the heterogeneous SOM distributions, although the influence of space weathering cannot be completely excluded. Effects of the space weathering on organic species and its heterogeneity on extraterrestrial samples should be investigated to reveal more detailed mechanisms to produce heterogeneous distribution of SOM on Ryugu sample.

#### Different spatial distribution of alkyl homologues of SOMs

A range of alkylated homologues was identified for CHN compounds in A0080 and was previously reported from Murchison, Murray (CM2), and Yamato 002540 (CR) (Naraoka et al. 2017; Naraoka and Hashiguchi 2018; Hashiguchi and Naraoka 2019b; Isa et al. 2021), but not identified from Orgueil in this study.

The reaction of aldehydes and ammonia through aldol condensation reactions has been proposed for the formation and growth of alkylated N-heterocycles including alkyl-pyridines in CCs (Yamashita and Naraoka 2014; Naraoka et al. 2017). On the other hand, Isa et al. (2021) suggested that the mass distribution of SOM in Tagish Lake samples cannot be explained by such a condensation

process. Instead, they proposed that the complex features of the SOM were established before accretion on the parent body followed by simplification in the asteroid due to secondary processes such as aqueous alteration. Orgueil showed similar characteristics to CI and shows an extensive degree of aqueous alteration. According to argument by Isa et al. (2021) this result may indicate that the CHN compounds in A0080 have relatively been unaffected by aqueous alteration compared to that in Orgueil.

Abundance of alkyl homologues of CHN compounds (also other SOMs) in lithology 1 and lithology 2 of A0080 were not significantly different (Fig. 6). On the other hand, carbonate-rich fragment 1 was enriched in  $C_nH_mN$  compounds with a larger C number in Murchison (Fig. 13). Furthermore, a clearly different distribution of  $C_nH_mN$  and  $C_nH_mN_2$  compounds implies either (1) different formation pathway to form these compounds or (2) different interactions with minerals (e.g., carbonate grains). The specific relationships between minerals were not identified; therefore, a detailed mechanism for the correlation in the physical distributions of  $C_nH_mN$  and  $C_nH_mN_2$  compounds in these samples is elusive. And yet, that distinct feature between Murchison and A0080 is remarkable and implies that the formation mechanism for the alkylated homologues of CHN compounds may be different between Murchison and A0080. This result implies a primordial feature of CHN compounds in A0080 described above or different formation or evolution (growth) mechanisms for the alkylated homologues of CHN compounds, for example during aqueous alteration (Naraoka et al. 2017).

Orthous-Daunay et al. (2019) suggested that the Murchison meteorite appeared to be formed where the UV photon flux was negligible, or it has been accreted and shielded from photolysis in the parent body. However, some chemical processes during fluid activity appeared to be more likely than the effect of space weathering for the distinct feature of alkylated CHN homologues between Murchison and A0080 because the positive relationship of carbonate abundance of carbonate was observed in both samples.

#### Molecular distribution by ToF–SIMS

Organic-related ions detected by ToF–SIMS showed different abundances among area C within lithology 1, and area A within lithology 2 and around those boundaries (area B) (Fig. 7). The intensities of these ions from three regions were similar, and highest in area C. DESI–HRMS imaging found abundant CHO compounds and lower abundances of CHN or CHNO compounds in area C than in area A and area B, which is inconsistent with the occurrence of  $CNO^+$ ,  $CHNO^+$ , and  $CN^-$  ions by ToF–SIMS analysis. Carboxylate ions ( $CO_3^{2-}$ ,  $CO_4^-$ ,

and probably  $\text{RCO}_2^-$ ) appeared to be consistent with the result of DESI-HRMS imaging results, even if they could be derived from CHO compounds or dolomite grains.

Inconsistency of spatial distribution for organic species between ToF-SIMS data and DESI-HRMS imaging data for spatial distribution of organic species is probably the result of different ionization mechanisms between ToF-SIMS (sputtering by the ion beam) and DESI-HRMS imaging (desorption and ionization by charged solvent spray). Although soluble organic matter such as amino acids can be analyzed by ToF-SIMS (Noun et al. 2019), our result may indicate that ions detected from A0080 by ToF-SIMS would be mostly derived from methanol-insoluble organic compounds. Such organic compounds include IOM, which contains several functional groups including C=O and C=C (Yabuta et al. 2023). In addition, SOM in Tagish Lake meteorite, was sufficiently detected even after 2–3 repeated measurements of DESI-HRMS using same analytical condition, which may be because of organic matter is associated with clay minerals (Hashiguchi and Naraoka 2019a). Therefore, SOM could be consumed during DESI-HRMS analysis from sample surface, however it is unlikely that SOM in A0080 was completely lost by DESI-HRMS in this study. More than that, our result can probably be explained by that organic ions detected by ToF-SIMS are mostly fragmented ones from parent organic ions whereas DESI causes minimum fragmentation (Cooks et al. 2006). Furthermore, methanol-insoluble organic matter such as IOM (Laurent et al. 2022) would be detected by ToF-SIMS, on the other hand, only methanol-soluble compounds can be detected by DESI-HRMS. These differences could have led to the incongruent results between TOF-SIMS and DESI-HRMS observed in A0080. Further *in-situ* coordinated analysis using ToF-SIMS is expected to reveal the relationship between SOM, IOM, and minerals in asteroid Ryugu.

## Summary and Conclusion

We performed *in-situ* analysis on a Ryugu sample A0080 using the DESI-HRMS imaging, ToF-SIMS, and mineralogical observation by FE-SEM-EDS to investigate the relationship of organic compounds to minerals. Our result shows the following:

- (1) Different spatial distributions of SOM were observed on the surface of Ryugu grain A0080, which are assigned as CHN, CHO, CHO-Na, and CHNO in A0080 across a few hundred  $\mu\text{m}$ . The distribution could be due to different timing of precipitation of these SOM from the aqueous fluid during fluid flow and consumption on the asteroid Ryugu, or to different transportation by aqueous fluid.

- (2) Heterogeneous distribution among the same alkylated homologues ( $-\text{CH}_2-$ families) of the SOMs was identified in A0080. Alkylated CHN compounds are also abundant in Murchison and more enriched in a fragment with abundant carbonates. The alkylated CHN compounds were not identified in Orgueil. Relationship between abundance of the alkylated CHN compounds and altered minerals including carbonates were not clear in A0080 different from Murchison. These results indicate that the formation or growth mechanism for the alkylated homologues of CHN compounds during aqueous alteration between Murchison and A0080 was different. Such a difference seemed to be attributed to the presence of carbonate grains, particularly Ca carbonate, which may have been catalyst for alkylation of CHN compounds. Alternatively, our result implies more primordial feature (less affected by aqueous alteration) of CHN compounds in A0080 than in Murchison and Orgueil.
- (3) Spatial distribution of SOM in A0080 revealed by DESI-HRMS imaging was not consistent with the abundance of CN, CNO, or CHNO ions measured by ToF-SIMS, whereas carboxylate-ions detected by ToF-SIMS seemed to be consistent with DESI-HRMS data. This result indicates that TOF-SIMS detects mainly fragment ions, whereas DESI-HRMS detects SOM almost without fragmentation, or that the ToF-SIMS analysis has probably detected molecules mostly from methanol-insoluble organic matter, including IOM, on the surface of A0080.

## Supplementary Information

The online version contains supplementary material available at <https://doi.org/10.1186/s40623-023-01792-w>.

**Additional file 1. Figure S1.** Photograph of the initial sample A0080 (total 1.4 mg) collected from the first touchdown at asteroid Ryugu. The photos were taken in the clean chamber of the ISAS/JAXA curation facility before sample distribution. **Figure S2.** Left: combined image of BSE image of A0080 and RGB image of total CHO (red), total CHN (green), and total CHNO compounds. Right: topography image obtained from the almost the same area as the SE image. The color bar shows a depth of the sample surface ranged from 0–339  $\mu\text{m}$ . The dotted line shows the highest region on the surface, which is roughly corresponding to the SOM concentrated region identified by DESI-HRMS imaging. **Figure S3.** Evaluation of effect for ion intensity of DESI-HRMS imaging using an epoxy. (a) An optical microscope image of epoxy with scratches of different roughness. (b) A DESI image of  $m/z$  368.428 ( $\text{C}_{25}\text{H}_{54}\text{N}^+$ ) from the epoxy surface. Outline of white dotted line corresponds to a region for normalization of ion intensity. (c) Normalized image using averaged ion intensity obtained from a region shown by dotted rectangle in (b). White solid rectangles correspond to areas 1, 2, and 3 surrounding scratches with different roughness described in (a). Correlation between decrease of ion intensity and (d) difference of depth from the surface region used for normalization or (e) width of scratches. **Figure S4.** (a) A BSE image and positive secondary ion images obtained by TOF-SIMS from area A in Fig. 7. (b) An BSE image and negative secondary ion images obtained by TOF-SIMS from area B in

Fig. 7. All scale bars show 100  $\mu\text{m}$ . Color bars show ion counts. Note that the positioning of the TOF-SIMS images and BSE image contains a  $\sim \pm 20$   $\mu\text{m}$  uncertainty. **Figure S5.** Left: BSE image of the Orgueil meteorite with color outlines for SOM concentrated regions (pink, green, blue, and yellow corresponds to CHO, CHN, CHNO, and CHO-Na compounds, respectively). The white dotted line shows the regions of highest SOM concentrations. Right: topographic image obtained from almost the same area as the BSE image. The color bar shows a depth of the sample surface ranged from 0–115  $\mu\text{m}$ . **Figure S6.** A comparison of ESI efficiency from Flow Injection Analysis (FIA)-HRMS and DESI-HRMS desorption efficiency on various organic reagents. All ions correspond to  $[\text{M}+\text{H}]^+$ . The ion intensities from DESI-HRMS data were calculated from 2 mm  $\times$  2 mm for each ion images. Error bars correspond 2 $\sigma$ , which were calculated using standard deviation of the eluent blank data for FIA-HRMS data, or standard deviation of pixels in analyzed area for DESI-HRMS data. Experimental conditions are described below. **Table S1.** Comparison of ESI efficiency and DESI desorption efficiency on organic reagents.

### Acknowledgements

The Hayabusa2 project has been led by JAXA (Japan Aerospace Exploration Agency) in collaboration with DLR (German Space Center) and CNES (French Space Center) and supported by NASA and ASA (Australian Space Agency). We are grateful to all the members of the Hayabusa2 project for their technical and scientific contributions. We sincerely thank Dr. Conel M.O'D. Alexander, an anonymous reviewer, and the editors of EPS for their constructive comments.

### Author contributions

MH contributed to sample preparation, DESI-HRMS analysis, and mineralogical observation by FE-SEM-EDS, 3D-laser microscope observation, data processing and interpretation, and manuscript preparation. DA operated ToF-SIMS analysis and DA and KF contributed to ToF-SIMS data interpretation. HN contributed to data interpretation. HN, YT, JPD designed the implementation of the SOM scheme and the initial analysis timelines ( $\sim$ 31-May-2022). All authors contributed to the writing and editing of the manuscript.

### Funding

The research is partly supported by JSPS KAKENHI Grant Numbers JP21K03641 for MH, JP20H00202 and JP20H05846 for HN, and JP18H03959 for DA and KF; and NASA Consortium for Hayabusa2 Analysis of Organic Solubles for JPD, JCA, JEE, DPG, HVG, HLM, and ETP.

### Data availability

The data used in this study are available from the corresponding author on reasonable request.

### Declarations

### Competing interests

The authors declare that they have no competing interests.

### Author details

<sup>1</sup>Graduate School of Environmental Studies, Nagoya University, Furo-Cho, Chikusa-Ku, Nagoya 464-8601, Japan. <sup>2</sup>Graduate School of Bioagricultural Sciences, Nagoya University, Furo-Cho, Chikusa-Ku, Nagoya 464-8601, Japan. <sup>3</sup>Department of Earth and Planetary Sciences, Kyushu University, Motooka 744, Nishi-Ku, Fukuoka 819-0395, Japan. <sup>4</sup>Biogeochemistry Research Center (BGC), Japan Agency for Marine-Earth Science and Technology (JAMSTEC), 2-15 Natsushima, Yokosuka 237-0061, Japan. <sup>5</sup>Solar System Exploration Division, NASA Goddard Space Flight Center, Greenbelt, MD 20771, USA. <sup>6</sup>Anne Arundel Community College, Arnold, MD 21012, USA. <sup>7</sup>Division of Geological and Planetary Sciences, California Institute of Technology, Pasadena, CA 91125, USA. <sup>8</sup>Department of Earth Material Science, Tohoku University, Aoba-Ku, Sendai 980-8578, Japan. <sup>9</sup>Graduate School of Pharmaceutical Sciences, Kyushu University, Motooka 744, Nishi-Ku, Fukuoka 819-0395, Japan. <sup>10</sup>Helmholtz Zentrum München, Analytical BioGeoChemistry, Ingolstaedter Landstraße 1, 85764 Neuherberg, Germany. <sup>11</sup>Earth-Life Science Institute (ELSI), Tokyo Institute of Technology, Meguro-ku, Tokyo 152-8550, Japan. <sup>12</sup>Center for Research and Exploration in Space Science and Technology

(CRESST), NASA GSFC, Greenbelt, MD, USA. <sup>13</sup>Department of Life, Environment and Applied Chemistry, Fukuoka Institute of Technology, Higashi-ku, Fukuoka 811-0295, Japan. <sup>14</sup>Institute of Low Temperature Science (ILTS), Hokkaido University, Kita-ku, Sapporo 060-0810, Japan. <sup>15</sup>Université Grenoble Alpes, CNRS, IPAG, 38000 Grenoble, France. <sup>16</sup>CNRS, Laboratoire de Physique des Interactions Ioniques et Moléculaires, Université Aix-Marseille, 13397 Marseille, France. <sup>17</sup>Department of Chemistry and Pharmacy, Ludwig-Maximilians-University, 81377 Munich, Germany. <sup>18</sup>Excellence Cluster ORIGINS, 85748 Garching, Germany. <sup>19</sup>Technische Universität München, Analytische Lebensmittel Chemie, Maximus-von-Forum 2, 85354 Freising, Germany. <sup>20</sup>Institute of Space and Astronautical Science, Japan Aerospace Exploration Agency (ISAS/JAXA), Sagami-hara 252-5210, Japan. <sup>21</sup>CNRS, Institut de Chimie Physique, UMR8000, Université Paris-Saclay, 91405 Orsay, France. <sup>22</sup>Department of Earth and Planetary Sciences, Hokkaido University, Kita-ku, Sapporo 060-0810, Japan. <sup>23</sup>Division of Earth and Planetary Sciences, Kyoto University, Kitashirakawa-iwake-cho, Sakyo-ku, Kyoto 606-8502, Japan. <sup>24</sup>Department of Earth and Planetary Sciences, Kyushu University, Motooka 744, Nishi-ku, Fukuoka 819-0395, Japan. <sup>25</sup>Department of Earth and Planetary Sciences, Hiroshima University, Higashi-Hiroshima, Hiroshima 739-8526, Japan. <sup>26</sup>UTokyo Organization for Planetary and Space Science, University of Tokyo, Bunkyo-ku, Tokyo 113-0033, Japan. <sup>27</sup>Institute of Space and Astronautical Science (ISAS), Japan Aerospace Exploration Agency (JAXA), Sagami-hara 252-5210, Japan. <sup>28</sup>Kanagawa Institute of Technology, Atsugi 243-0292, Japan.

Received: 3 July 2022 Accepted: 27 February 2023

Published online: 08 May 2023

### References

- Aponte JC, Dworkin JP, Glavin DP, Elsila JE, Parker ET, McLain HL, Naraoka H, Okazaki R, Takano Y, Tachibana S, Dong G, Zeichner SS, Eiler JM, Yurimoto H, Nakamura T, Yabuta H, Terui F, Noguchi T, Sakamoto K, Yada T, Nishimura M, Nakato A, Miyazaki A, Yogata K, Abe M, Okada T, Usui T, Yoshikawa M, Saiki T, Tanaka S, Nakazawa S, Tsuda Y, Watanabe S, The Hayabusa2-initial-analysis SOM team, and The Hayabusa2-initial-analysis core team (2023) Earth Planets Space 75:28. <https://doi.org/10.1186/s40623-022-01758-4>
- Awad AM, Shaikh SMR, Jalab R, Gulied MH, Nasser MS, Benamor A, Adham S (2019) Adsorption of organic pollutants by natural and modified clays: A comprehensive review. Sep Purif Technol 228:39. <https://doi.org/10.1016/j.seppur.2019.115719>
- Barosch J, Nittler LR, Wang J, Alexander CMO'D, De Gregorio BT, Engrand C, Kebukawa Y, Nagashima K, Stroud RM, Yabuta H, Abe Y, Aléon J, Amari S, Amelin Y, Bajo K, Bejach L, Bizzarro M, Bonal L, Bouvier A, Carlson RW, Chaussidon M, Choi B-G, Cody GD, Dartois E, Dauphas N, Davis AM, Dazzi A, Deniset-Besseau A, Di Rocco T, Duprat J, Fujiya W, Fukai R, Gautam I, Haba MK, Hashiguchi M, Hibiya Y, Hidaka H, Homma H, Hoppe P, Huss GR, Ichida K, Iizuka T, Ireland TR, Ishikawa A, Ito M, Itoh S, Kamide K, Kawasaki N, Kilcoyne DAL, Kita NT, Kitajima K, Kleine T, Komatani S, Komatsu M, Krot AN, Liu M-C, Martins Z, Masuda Y, Mathurin J, McKeegan KD, Montagnac G, Morita M, Mostefaoui S, Motomura K, Moynier F, Nakai I, Nguyen AN, Ohigashi T, Okumura T, Onose M, Pack A, Park C, Piani L, Qin L, Quirico E, Remusat L, Russell SS, Sakamoto N, Sandford SA, Schönbacher M, Shigenaka M, Suga H, Tafla L, Takahashi Y, Takeichi Y, Tamenori Y, Tang H, Terada K, Terada Y, Usui T, Verdier-Paoletti M, Wada S, Wadhwa M, Wakabayashi D, Walker RJ, Yamashita K, Yamashita S, Yin Q-Z, Yokoyama T, Yoneda S, Young ED, Yui H, Zhang A-C, Abe M, Miyazaki A, Nakato A, Nakazawa S, Nishimura M, Okada T, Saiki T, Tanaka S, Terui F, Tsuda Y, Watanabe S, Yada T, Yogata K, Yoshikawa M, Nakamura T, Naraoka H, Noguchi T, Okazaki R, Sakamoto K, Tachibana S, and Yurimoto H (2022) Presolar stardust in asteroid Ryugu. *Astrophys J Lett* 935:L3. <https://doi.org/10.3847/2041-8213/ac83bd>
- Bland PA, Jackson MD, Coker RF, Cohen BA, Webber JB, Lee MR, Duffy CM, Chater RJ, Ardakani MG, McPhail DS, McComb DW, Benedix GK (2009) Why aqueous alteration in asteroids was isochemical: High porosity  $\neq$  high permeability. *Earth Planet Sci Lett* 287:559–568. <https://doi.org/10.1016/j.epsl.2009.09.004>
- Bockelée-Morvan D, Biver N (2017) The composition of cometary ices. *Philos Trans R Soc Lond A* 375:11. <https://doi.org/10.1098/rsta.2016.0252>

- Bolger JC (1983) Acid base interactions between oxide surfaces and polar organic compounds. In Mittal KL (eds) *Adhesion aspects of polymeric coatings*. Springer, pp 3–18. [https://doi.org/10.1007/978-1-4613-3658-7\\_1](https://doi.org/10.1007/978-1-4613-3658-7_1)
- Brearely AJ (1995) Aqueous alteration and brecciation in Bells, an unusual, saponite-bearing, CM chondrite. *Geochim Cosmochim Acta* 59:2291–2317. [https://doi.org/10.1016/0016-7037\(95\)00107-B](https://doi.org/10.1016/0016-7037(95)00107-B)
- Brearely AJ (2006) Action of water. In: Lauretta DS, McSween Jr HY (eds) *Meteorites and the early solar system II*. University of Arizona Press, Tucson, pp. 584–624. <https://doi.org/10.2307/j.ctv1v7zdm.35>
- Carrier BL, Abbey WJ, Beegle LW, Bhartia R, Liu Y (2019) Attenuation of ultraviolet radiation in rocks and minerals: implications for mars science. *J Geophys Res Planets* 124:2599–2612. <https://doi.org/10.1029/2018JE005758>
- Chan QHS, Zolensky ME, Bodnar RJ, Farley C, Cheung JCH (2017) Investigation of organo-carbonate associations in carbonaceous chondrites by Raman spectroscopy. *Geochim Cosmochim Acta* 201:392–409. <https://doi.org/10.1016/j.gca.2016.10.048>
- Cooks RG, Ouyang Z, Takats Z, Wiseman JM (2006) Ambient mass spectrometry. *Science* 311:1566–1570. <https://doi.org/10.1126/science.1119426>
- Dickinson SR, McGrath KM (2003) Switching between kinetic and thermodynamic control: calcium carbonate growth in the presence of a simple alcohol. *J Mater Chem* 13:928–933. <https://doi.org/10.1039/B208741N>
- Dodson-Robinson SE, Willacy K, Bodenheimer P, Turner NJ, Beichman CA (2009) Ice lines, planetesimal composition and solid surface density in the solar nebula. *Icarus* 200:672–693. <https://doi.org/10.1016/j.icarus.2008.11.023>
- Fujiya W, Sugiura N, Sano Y, Hiyagon H (2013) Mn–Cr ages of dolomites in CI chondrites and the Tagish Lake ungrouped carbonaceous chondrite, Earth Planet. Sci Lett 362:130–142. <https://doi.org/10.1016/j.epsl.2012.11.057>
- Goesmann F, Rosenbauer H, Bredehöft JH, Cabane M, Ehrenfreund P, Gautier T, Giri C, Krüger H, Le Roy L, MacDermott AJ, McKenna-Lawlor S, Meierhenrich UJ, Muñoz Caro GM, Raulin F, Roll R, Steele A, Steininger H, Sternberg R, Szopa C, Thiemann W, and Ullamec S (2015) Organic compounds on comet 67P/Churyumov-Gerasimenko revealed by COSAC mass spectrometry. *Science* 349:aab0689. <https://doi.org/10.1126/science.aab0689>
- Gounelle M, Zolensky ME (2014) The Orgueil meteorite: 150 years of history. *Meteoritics Planet Sci* 49:1769–1794. <https://doi.org/10.1111/maps.12351>
- Hashiguchi M, Naraoka H (2019a) Abundant magnesium-containing organic compounds in the Tagish Lake meteorite. In: Abstracts of the 50th Lunar and Planetary Science Conference, The Woodlands, Texas, LPI Contribution No. 2132, id.1499
- Hashiguchi M, Naraoka H (2019b) High-mass resolution molecular imaging of organic compounds on the surface of Murchison meteorite. *Meteoritics Planet Sci* 54:452–468. <https://doi.org/10.1111/maps.13211>
- Hashizume H (2015) Adsorption of nucleic acid bases, ribose, and phosphate by some clay minerals. *Life* 5:637–650. <https://doi.org/10.3390/life5010637>
- Hopp T, Dauphas N, Abe Y, Aléon J, Alexander CMO'D, Amari S, Amelin Y, Bajo K, Bizzarro M, Bouvier A, Carlson RW, Chaussidon M, Choi B-G, Davis AM, Di Rocco T, Fujiya W, Fukai R, Gautam I, Haba MK, Hibiya Y, Hidaka H, Homma H, Hoppe P, Huss GR, Ichida K, Iizuka T, Ireland TR, Ishikawa A, Ito M, Itoh S, Kawasaki N, Kita NT, Kitajima K, Kleine T, Komatani S, Krot AN, Liu M-C, Masuda Y, McKeegan KD, Morita M, Motomura K, Moynier F, Nakai I, Nagashima K, Nesvorný D, Nguyen A, Nittler L, Onose M, Pack A, Park C, Piani L, Qin L, Russell SS, Sakamoto N, Schönbachler M, Tafla L, Tang H, Terada K, Terada Y, Usui T, Wada S, Wadhwa M, Walker RJ, Yamashita K, Yin Q-Z, Yokoyama T, Yoneda S, Young ED, Yui H, Zhang A-C, Nakamura T, Naraoka H, Noguchi T, Sakamoto K, Yabuta H, Abe M, Miyazaki A, Nakato A, Nishimura M, Okada T, Yada T, Yogata K, Nakazawa S, Saiki T, Tanaka S, Terui F, Tsuda Y, Watanabe S, Yoshikawa M, Tachibana S, and Yurimoto H (2022) Ryugu's nucleosynthetic heritage from the outskirts of the Solar System. *Sci Adv* 46:9. <https://doi.org/10.1126/sciadv.add8141>
- Howard KT, Benedix GK, Bland PA, Cressley G (2009) Modal mineralogy of CM2 chondrites by X-ray diffraction (PSD-XRD). Part 1: Total phyllosilicate abundance and the degree of aqueous alteration. *Geochim Cosmochim Acta* 73:4576–4589. <https://doi.org/10.1016/j.gca.2009.04.038>
- Ifa DR, Gumaelius LM, Eberlin LS, Manicke NE, Cooks RG (2007) Forensic analysis of inks by imaging desorption electrospray ionization (DESI) mass spectrometry. *Analyst* 132:461–467. <https://doi.org/10.1039/b700236j>
- Isa J, Orthous-Daunay F-R, Beck P, Herd CDK, Vuitton V, Flandinet L (2021) Aqueous alteration on asteroids simplifies soluble organic matter mixtures. *Astrophys J Lett* 920:L39. <https://doi.org/10.3847/2041-8213/ac2b34>
- Ito M, Tomioka N, Uesugi M, Yamaguchi A, Shirai N, Ohigashi T, Liu M-C, Greenwood RC, Kimura M, Imae N, Uesugi K, Nakato A, Yogata K, Yuzawa H, Kodama Y, Tsuchiyama A, Yasutake M, Findlay R, Franchi IA, Malley J A, McCain KA, Matsuda N, McKeegan KD, Hirahara K, Takeuchi A, Sekimoto S, Sakurai I, Okada I, Karouji Y, Arakawa M, Fujii A, Fujimoto M, Hayakawa M, Hirata N, Hirata N, Honda R, Honda C, Hosoda S, Iijima Y, Ikeda H, Ishiguro M, Ishihara Y, Iwata T, Kawahara K, Kikuchi S, Kitazato K, Matsumoto K, Matsuoka M, Michikami T, Mimasu Y, Miura A, Mori O, Morota T, Nakazawa S, Namiki N, Noda H, Noguchi R, Ogawa N, Ogawa K, Okada T, Okamoto C, Ono G, Ozaki M, Saiki T, Sakatani N, Sawada H, Senshu H, Shimaki Y, Shirai K, Sugita S, Takei Y, Takeuchi H, Tanaka S, Tatsumi E, Terui F, Tsukizaki R, Wada K, Yamada M, Yamada T, Yamamoto Y, Yano H, Yokota Y, Yoshihara K, Fukai R, Furuya S, Hatakeda K, Hayashi T, Hitomi Y, Kumagai K, Miyazaki A, Nishimura M, Soejima H, Iwamae A, Yamamoto D, Yoshitake M, Yada T, Abe M, Usui T, Watanabe S, and Tsuda Y (2022) A pristine record of outer Solar System materials from asteroid Ryugu's returned sample. *Nat. Astron.* 6:1163–1171. <https://doi.org/10.1038/s41550-022-01745-5>
- Kawasaki N, Nagashima K, Sakamoto N, Matsumoto T, Bajo K, Wada S, Igami Y, Miyake A, Noguchi T, Yamamoto D, Russell SS, Abe Y, Aléon J, Alexander CMO'D, Amari S, Amelin Y, Bizzarro M, Bouvier A, Carlson RW, Chaussidon M, Choi B-G, Dauphas N, Davis AM, Di Rocco T, Fujiya W, Fukai R, Gautam I, Haba MK, Hibiya Y, Hidaka H, Homma H, Hoppe P, Huss G, Ichida K, Iizuka T, Ireland T, Ishikawa A, Ito M, Itoh S, Kita NT, Kitajima K, Kleine T, Komatani S, Krot AN, Liu M-C, Masuda Y, McKeegan KD, Morita M, Motomura K, Moynier F, Nakai I, Nguyen A, Nittler L, Onose M, Pack A, Park C, Piani L, Qin L, Schönbachler M, Tafla L, Tang H, Terada K, Terada Y, Usui T, Wadhwa M, Walker RJ, Yamashita K, Yin Q-Z, Yokoyama T, Yoneda S, Young ED, Yui H, Zhang A-C, Nakamura T, Naraoka H, Okazaki R, Sakamoto K, Yabuta H, Abe M, Miyazaki A, Nakato A, Nishimura M, Okada T, Yada T, Yogata K, Nakazawa S, Saiki T, Tanaka S, Terui F, Tsuda Y, Watanabe S, Yoshikawa M, Tachibana S, and Yurimoto H (2022) Oxygen isotopes of anhydrous primary minerals show kinship between asteroid Ryugu and comet 81P/Wild2. *Sci Adv* 8:10. <https://doi.org/10.1126/sciadv.ade2067>
- Kebukawa Y, Nakashima S, Ishikawa M, Aizawa K, Inoue T, Nakamura-Messenger K, Zolensky ME (2010) Spatial distribution of organic matter in the Bells CM2 chondrite using near-field infrared microspectroscopy. *Meteorit Planet Sci* 45:394–405. <https://doi.org/10.1111/j.1945-5100.2010.01030.x>
- Kimura M, Sato T, Nakamura N, Nozawa J, Nakamura T, Tsukamoto K, Yamamoto K (2013) Vortex magnetic structure in frambooidal magnetite reveals existence of water droplets in an ancient asteroid. *Nat Geosci* 4:2649–2656. <https://doi.org/10.1038/ncomms3649>
- Laurent B, Remusat L, Viennet J-C, Brunetto R, Binet L, Holin M, Ciccio M, Bouvier C, Brunelle A, Bernard S (2022) Preservation of the isotope signatures in chondritic IOM during aqueous alteration. *Geochem Perspect Lett* 23:28–32
- Le Guillou C, Bernard S, Brearely AJ, Remusat L (2014) Evolution of organic matter in Orgueil Murchison and Renazzo during parent body aqueous alteration: in situ investigations. *Geochim Cosmochim Acta* 131:368–392. <https://doi.org/10.1016/j.gca.2013.11.020>
- Loizeau D, Pilorget C, Riu L, Brunetto R, Bibring JP, Nakato A, Aléon-Toppiani A, Hatakeda K, Yogata K, Carter J, Le Pivert-Jolivet T, Yada T, Okada T, Usui T, Langevin Y, Lantz C, Baklouti D, Miyazaki A, Nishimura M, Nagashima K, Kumagai K, Hitomi Y, Abe M, Saiki T, Tanaka S, Nakazawa S, Tsuda Y, and Watanabe S (2023) Constraints on solar system early evolution by Micro-mega analysis of Ryugu carbonates. *Nat Astron* 12:1. <https://doi.org/10.1038/s41550-022-01870-1>
- Muneishi K, Naraoka H (2021) Interactions between organic compounds and olivine under aqueous conditions: a potential role for organic distribution in carbonaceous chondrites. *Meteorit Planet Sci* 56:195–205. <https://doi.org/10.1111/maps.13614>
- Nakamura T, Matsumoto M, Amano K, Enokido Y, Zolensky M, Mikouchi T, Genda H, Tanaka S, Zolotov M, Kurosawa K, Wakita S, Hyoudo R, Nagano H, Nakashima D, Takahashi Y, Fujioka Y, Kikui M, Kagawa E, Matsuoka M, Brearely A, Tsuchiyama A, Uesugi M, Matsuno J, Kimura Y, Sato M, Milliken M, Tatsumi E, Sugita S, Hiroi T, Kitazono K, Brownlee D, Joswiak D, Takahashi M, Ninomiya K, Osawa T, Terada K, Brenker F, Tkalcic B, Vincze L, Brunetto R, Aléon-Toppiani A, Chan Q, Roskosz M, Vinnet J, Beck P, Alp E, Michikami

- T, Nagaashi Y, Tsuji T, Ino Y, Martinez J, Han J, Dolocan H, Bodnar R, Tanaka M, Yoshida H, Sugiyama K, King A, Fukushi K, Suga H, Yamashita S, Kawai T, Inoue K, Nakato A, Noguchi T, Vilas F, Hendrix A, Jaramillo C, Lorin D, Dominguez G, Gainsforth Z, Engrand C, Duprat J, Russell S, Bonato E, Ma C, Kawamoto T, Wada T, Watanabe S, Endo R, Enju S, Riu L, Rubino S, Tack P, Takeshita S, Takeichi Y, Takeuchi A, Takigawa A, Takir D, Tanigaki T, Taniguchi A, Tsukamoto K, Yagi T, Yamada S, Yamamoto K, Yamashita Y, Yasutake M, Uesugi K, Umegaki K, I-Huan C, Ishizaki Y, Okumura S, Palomba E, Pilorget C, Potin S, Abdulkareem A, Anada S, Araki Y, Sakatani N, Schulz C, Sekizawa O, Sitzman S, Sugiura K, Sun M, Dartois E, De Pauw E, Dionnet Z, Djouadi Z, Falkenberg G, Fujita R, Fukuma T, Gearba I, Hagiya K, Hu M, Kato T, Kawamura T, Kimura M, Kubo M, Langenhorst F, Lantz C, Lavina B, Lindner M, Vekemans B, Baklouti D, Bazi B, Borondics F, Nagasawa S, Nishiyama G, Nitta K, Mathurin J, Matsumoto T, Mitsukawa I, Miura H, Miyake A, Miyake Y, Yurimoto H, Okazaki R, Yabuta H, Naraoka H, Sakamoto K, Tachibana S, Connolly Jr D, Lauretta D, Yoshitake M, Yoshikawa M, Yoshihara K, Yokota Y, Yogata K, Yano H, Yamamoto Y, Yamamoto D, Yamada M, Yada T, Wada K, Usui T, Tsukizaki R, Terui F, Takeuchi H, Takei Y, Suzuki A, Soejima H, Shirai K, Shimaki Y, Senshu H, Sawada H, Saiki T, Ozaki M, Ono G, Okada T, Ogawa N, Ogawa K, Noguchi R, Noda H, Nishimura M, Namiki N, Nakazawa S, Morota T, Miyazaki A, Miura A, Mimitsu Y, Matsumoto K, Kumagai K, Kouyama T, Kikuchi S, Kawahara K, Kameda S, Iwata T, Ishihara Y, Ishiguro M, Ikeda H, Hosoda S, Honda R, Honda C, Hitomi Y, Hirata N, Hirata N, Hayakawa M, Hatakeda K, Furuya S, Fukai R, Fujii A, Cho Y, Arakawa M, Abe M, Watanabe S, and Tsuda Y (2022) Formation and evolution of carbonaceous asteroid Ryugu: Direct evidence from returned samples. *Science* 379:eabn8671. <https://doi.org/10.1126/science.abn8671>
- Naraoka H, Hashiguchi M (2018) In situ organic compound analysis on a meteorite surface by desorption electrospray ionization coupled with an Orbitrap mass spectrometer. *Rapid Commun Mass Spectrom* 32:959–964. <https://doi.org/10.1002/rcm.8121>
- Naraoka H, Yamashita Y, Yamaguchi M, Orthous-Daunay F-R (2017) Molecular evolution of N-containing cyclic compounds in the parent body of the Murchison Meteorite. *ACS Earth Space Chem* 1:540–550. <https://doi.org/10.1021/acsearthspacechem.7b00058>
- Naraoka H, Takano Y, Dworkin JP, Oba Y, Hamase K, Furusho A, Ogawa NO, Hashiguchi M, Fukushima K, Aoki D, Schmitt-Kopplin P, Aponte JC, Parker ET, Glavin DP, McLain HL, Elsil JA, Graham HV, Eiler JM, Orthous-Daunay F-R, Wolters C, Isa J, Vuitton V, Thissen R, Sakai S, Yoshimura T, Koga T, Ohkouchi N, Chikaraishi Y, Sugahara H, Mita H, Furukawa Y, Hertkorn N, Ruf A, Yurimoto H, Nakamura T, Noguchi T, Okazaki R, Yabuta H, Sakamoto K, Tachibana S, Connolly HC Jr, Lauretta DS, Abe M, Yada T, Nishimura M, Yogata K, Nakato A, Yoshitake M, Suzuki A, Miyazaki A, Furuya S, Hatakeda K, Soejima H, Hitomi Y, Kumagai K, Usui T, Hayashi T, Yamamoto D, Fukai R, Kitazato K, Sugita S, Namiki N, Arakawa M, Ikeda H, Ishiguro M, Hirata N, Wada K, Ishihara Y, Noguchi R, Morota T, Sakatani N, Matsumoto K, Senshu H, Honda R, Tatsumi E, Yokota Y, Honda C, Michikami T, Matsuoka M, Miura A, Noda H, Yamada T, Yoshihara K, Kawahara K, Ozaki M, Iijima Y, Yano H, Hayakawa M, Iwata T, Tsukizaki R, Sawada H, Hosoda S, Ogawa K, Okamoto C, Hirata N, Shirai K, Shimaki Y, Yamada M, Okada T, Yamamoto Y, Takeuchi H, Fujii A, Takei Y, Yoshikawa K, Mimasu Y, Ono G, Ogawa N, Kikuchi S, Nakazawa S, Terui F, Tanaka S, Saiki T, Yoshikawa M, Watanabe S, and Tsuda Y (2023) Soluble organic molecules in samples of the carbonaceous asteroid (162173) Ryugu. *Science* 379:eabn9033. <https://doi.org/10.1126/science.abn9033>
- Noguchi T, Matsumoto T, Miyake A, Igami Y, Haruta M, Saito H, Hata S, Seto Y, Miyahara M, Tomioka N, Ishii HA, Bradley JP, Ohtaki KK, Dobrică E, Leroux H, Le Guillou C, Jacob D, de la Peña F, Laforet S, Marinova M, Langenhorst F, Harries D, Beck P, Phan THV, Rebois R, Abreu NM, Gray J, Zega T, Zanetta P-M, Thompson MS, Stroud R, Burgess K, Cymes BA, Bridges JC, Hicks L, Lee MR, Daly L, Bland PA, Zolensky ME, Frank DR, Martinez J, Tsuchiyama A, Yasutake M, Matsuno J, Okumura S, Mitsukawa I, Uesugi K, Uesugi M, Takeuchi A, Sun M, Enju S, Takigawa A, Michikami T, Nakamura T, Matsumoto M, Nakauchi Y, Abe M, Arakawa M, Fujii A, Hayakawa M, Hirata N, Hirata N, Honda R, Honda C, Hosoda S, Iijima Y, Ikeda H, Ishiguro M, Ishihara Y, Iwata T, Kawahara K, Kikuchi S, Kitazato K, Matsumoto K, Matsuoka M, Mimasu Y, Miura A, Morota T, Nakazawa S, Namiki N, Noda H, Noguchi R, Ogawa N, Ogawa K, Okada T, Okamoto C, Ono G, Ozaki M, Saiki T, Sakatani N, Sawada H, Senshu H, Shimaki Y, Shirai K, Sugita S, Takei Y, Takeuchi H, Tanaka S, Tatsumi E, Terui F, Tsukizaki R, Wada K, Yamada M, Yamada T, Yamamoto Y, Yano H, Yokota Y, Yoshihara K, Yoshikawa M, Yoshikawa K, Fukai R, Furuya S, Hatakeda K, Hayashi T, Hitomi Y, Kumagai K, Miyazaki A, Nakato A, Nishimura M, Soejima H, Suzuki AI, Usui T, Yada T, Yamamoto D, Yogata K, Yoshitake M, Connolly HC Jr, Lauretta DS, Yurimoto H, Nagashima K, Kawasaki N, Sakamoto N, Okazaki R, Yabuta H, Naraoka H, Sakamoto K, Tachibana S, Watanabe S, and Tsuda Y (2022) A dehydrated space-weathered skin cloaking the hydrated interior of Ryugu. *Nat Astron* 7: 170–181. <https://doi.org/10.1038/s41550-022-01841-6>
- Noun M, Baklouti D, Brunetto R, Borondics F, Calligaro T, Dionnet Z, Le Sergeant d'HL, Nsouli B, Ribaud I, Roumie M, Della-Negra S (2019) A mineralogical context for the organic matter in the paris meteorite determined by a multi-technique analysis. *Life* 9(2):44. <https://doi.org/10.3390/life9020044>
- Oba Y, Takano Y, Furukawa Y, Koga T, Glavin DP, Dworkin JP, and Naraoka H (2022) Identifying the wide diversity of extraterrestrial purine and pyrimidine nucleobases in carbonaceous meteorites. *Nat Commun* 13:2008. <https://doi.org/10.1038/s41467-022-29612-x>
- Oba Y, Koga T, Takano Y, Ogawa NO, Ohkouchi N, Sasaki K, Sato H, Glavin DP, Dworkin JP, Naraoka H, Tachibana S, Yurimoto H, Nakamura T, Noguchi T, Okazaki R, Yabuta H, Sakamoto K, Yada T, Nishimura M, Nakato A, Miyazaki A, Yogata K, Abe M, Okada T, Usui T, Yoshikawa M, Saiki T, Tanaka S, Terui F, Nakazawa S, Watanabe S, Tsuda Y, and Hayabusa2-initial-analysis SOM team (2023) Uracil in the carbonaceous asteroid (162173) Ryugu. *Nat Commun* 14:1292. <https://doi.org/10.1038/s41467-023-36904-3>
- Orthous-Daunay F-R, Piani L, Flandinet L, Thissen R, Wolters C, Vuitton V, Poch O, Moynier F, Sugawara I, Naraoka H, Tachibana S (2019) Ultraviolet-photon fingerprints on chondritic large organic molecules. *Geochem J* 53:21–32. <https://doi.org/10.2343/geochemj.20544>
- Parker ET, McLain HL, Glavin DP, Dworkin JP, Elsil JA, Aponte JC, Naraoka H, Takano Y, Tachibana S, Yabuta H, Yurimoto H, Sakamoto K, Yada T, Nishimura M, Nakato A, Miyazaki A, Yogata K, Abe M, Okada T, Usui T, Yoshikawa M, Saiki T, Tanaka S, Nakazawa S, Tsuda Y, Terui F, Noguchi T, Okazaki R, Watanabe S, and Nakamura T (2023) Extraterrestrial amino acids and amines identified in Asteroid Ryugu samples returned by the Hayabusa2 mission. *Geochim Cosmochim Acta* 347: 42–57. <https://doi.org/10.1016/j.gca.2023.02.017>
- Pearson VK, Sephton MA, Kearsley AT, Bland PA, Franchi IA, Gilmour I (2002) Clay mineral-organic matter relationships in the early solar system. *Meteorit Planet Sci* 37:1829–1833. <https://doi.org/10.1111/j.1945-5100.2002.tb01166.x>
- Piani L, Tachibana S, Hama T, Tanaka H, Endo Y, Sugawara I, Dessimoulie L, Kimura Y, Miyake A, Matsuno J, Tsuchiyama A, Fujita K, Nakatsubo S, Fukushi H, Mori S, Chigai T, Yurimoto H, Kouchi A (2017) Evolution of morphological and physical properties of laboratory interstellar organic residues with ultraviolet irradiation. *Astrophys J* 835:11. <https://doi.org/10.3847/1538-4357/aa5ca6>
- Pilorget C, Okada T, Hamm VR, Brunetto R, Yada D, Loizeau L, Riu T, Usui A, Moussi-Soffys K, Hatakeda A, Nakato K, Yogata M, Abe A, Aléon-Toppani J, Carter M, Chaigneau B, Crane B, Gondet K, Kumagai Y, Langevin C, Lantz TL, Pivert-Jolivet G, Lequertier L, Lourit A, Miyazaki M, Nishimura F, Poulet M, Arakawa N, Hirata K, Kitazato S, Nakazawa N, Namiki T, Saiki S, Sugita S, Tachibana S, Tanaka M, Yoshikawa Y, Tsuda SW, Bibring J-P (2021) First compositional analysis of Ryugu samples by the MicrOmega hyperspectral microscope. *Nat Astron* 6:221–225. <https://doi.org/10.1038/s41550-021-01549-z>
- Potzsil C, Tanaka R, Ota T, Kunihiko T, Kobayashi K, Nakamura E (2020) Concentration of meteoritic free organic matter by fluid transport and adsorption. *Geochem Perspect Lett* 13:30–35. <https://doi.org/10.7185/geochemlet.2010>
- Roberts JA, Kenward PA, Fowle DA, Goldstein RH, Gonzalez LA, Moore DS (2013) Surface chemistry allows for abiotic precipitation of dolomite at low temperature. *Proc Natl Acad Sci USA* 110:14540–14545. <https://doi.org/10.1073/pnas.1305403110>
- Ruf A, Kanawati B, Hertkorn N, Yin Q-Z, Moritz F, Harir M, Lucio M, Michalke B, Wimpenny J, Shilobreeva S, Bronsky B, Saraykin V, Gabelica Z, Gougeon RD, Quirico E, Ralew S, Jakubowski T, Haack H, Gonsior M, Jenniskens P, Hinman NW, Schmitt-Kopplin P (2017) Previously unknown class of metalorganic compounds revealed in meteorites. *Proc Natl Acad Sci USA* 114:2819–2824. <https://doi.org/10.1073/pnas.1616019114>
- Schmitt-Kopplin P, Gabelica Z, Gougeon RD, Fekete A, Kanawati B, Harir M, Gebefuegi I, Eckel G, Hertkorn N (2010) High molecular diversity of extraterrestrial organic matter in Murchison meteorite revealed 40 years after its fall. *Proc Natl Acad Sci USA* 107:2763–2768. <https://doi.org/10.1073/pnas.0912157107>
- Tachibana S, Abe M, Arakawa M, Fujimoto M, Iijima Y, Ishiguro M, Kitazato K, Kobayashi N, Namiki N, Okada T, Okazaki R, Sawada H, Sugita S, Takano Y, Tanaka S, Watanabe S, Yoshikawa M, Kuninaka H, and The Hayabusa2 Project Team (2014) Hayabusa2: Scientific importance of samples returned from C-type



- near-Earth asteroid (162173) 1999 JU<sub>3</sub>. *Geochem J* 48:571–587. <https://doi.org/10.2343/geochemj.20350>
- Tachibana S, Sawada H, Okazaki R, Takano Y, Sakamoto K, Miura YN, Okamoto C, Yano H, Yamanouchi S, Michel P, Zhang Y, Schwartz S, Thuillet F, Yurimoto H, Nakamura T, Noguchi T, Yabuta H, Naraoka H, Tsuchiyama A, Imae N, Kurosawa K, Nakamura AM, Ogawa K, Sugita S, Morota T, Honda R, Kameda S, Tatsumi E, Cho Y, Yoshioka K, Yokota Y, Hayakawa M, Matsuoka M, Sakatani N, Yamada M, Kouyama T, Suzuki H, Honda C, Yoshimitsu T, Kubota Y, Demura H, Yada T, Nishimura M, Yogata K, Nakato A, Yoshitake M, Suzuki AI, Furuya S, Hatakeda K, Miyazaki A, Kumagai K, Okada T, Abe M, Usui T, Ireland TR, Fujimoto M, Yamada T, Arakawa M, Connolly HC, Fujii A, Hasegawa S, Hirata N, Hirata N, Hirose C, Hosoda S, Iijima Y, Ikeda H, Ishiguro M, Ishihara Y, Iwata T, Kikuchi S, Kitazato K, Lauretta DS, Libourel G, Marty B, Matsumoto K, Michikami T, Mimasu Y, Miura A, Mori O, Nakamura-Messenger K, Namiki N, Nguyen AN, Nittler LR, Noda H, Noguchi R, Ogawa N, Ono G, Ozaki M, Senshu H, Shimada T, Shimaki Y, Shirai K, Soldini S, Takahashi T, Takei Y, Takeuchi H, Tsukizaki R, Wada K, Yamamoto Y, Yoshikawa K, Yumoto K, Zolensky ME, Nakazawa S, Terui F, Tanaka S, Saiki T, Yoshikawa M, Watanabe S, and Tsuda Y (2022) Pebbles and sand on asteroid (162173) Ryugu: in situ observation and particles returned to Earth. *Science* 375:1011–1016. <https://doi.org/10.1126/science.abj8624>
- Tachibana S (2021) The Hayabusa2 mission: What will we expect from samples from C-type near-Earth asteroid (162173) Ryugu? In: Longobardo A (eds) *Sample return missions: The last Frontier of solar system exploration*. Elsevier, pp 142–162. <https://doi.org/10.1016/B978-0-12-818330-4.00007-0>
- Thomas MM, Clouse JA, Longo JM (1993) Adsorption of organic compounds on carbonate minerals: 1. Model compounds and their influence on mineral wettability. *Chem Geol* 109:201–213. [https://doi.org/10.1016/0009-2541\(93\)90070-Y](https://doi.org/10.1016/0009-2541(93)90070-Y)
- Thurman EM, Ferrer I, Barceló D (2001) Choosing between atmospheric pressure chemical ionization and electrospray ionization interfaces for the HPLC/MS analysis of pesticides. *Anal Chem* 73:5441–5449. <https://doi.org/10.1021/ac010506f>
- van Kooten EMME, Nagashima K, Kasama T, Wampfler S, Ramsey J, Frimann S, Balogh Z, Schiller M, Wielandt D, Franchi I, Jørgensen J, Krot A, Bizzarro M (2017) A divergent heritage for complex organics in Isheyevo lithic clasts. *Geochim Cosmochim Acta* 205:119–148. <https://doi.org/10.1016/j.gca.2017.02.002>
- Wada N, Kanamura K, Umegaki T (1999) Effects of carboxylic acids on calcite formation in the presence of Mg<sup>2+</sup> ions. *Adv Colloid Interface Sci* 212:357–364. <https://doi.org/10.1006/jcis.1998.6067>
- Wada N, Kanamura K, Umegaki T (2001) Effects of carboxylic acids on the crystallization of calcium carbonate. *Adv Colloid Interface Sci* 233:65–72. <https://doi.org/10.1006/jcis.2000.7215>
- Watanabe S, Tsuda Y, Yoshikawa M, Tanaka S, Saiki T, and Nakazawa S (2017) Hayabusa2 mission overview. *Space Sci Rev* 208:3–16. <https://doi.org/10.1007/s11214-017-0377-1>
- Wing MR, Bada JL (1991) The origin of the polycyclic aromatic hydrocarbons in meteorites. *Orig Life Evol Biosph* 21:375–383. <https://doi.org/10.1007/BF01808308>
- Yabuta H, Cody GD, Engrand C, Kebukawa Y, De Gregorio B, Bonal L, Remusat L, Stroud R, Quirico E, Nittler L, Hashiguchi M, Komatsu M, Okumura T, Mathurin J, Dartois E, Duprat J, Takahashi Y, Takeichi Y, Kilcoyne D, Yamashita S, Dazzi A, Deniset-Besseau A, Sandford S, Martins Z, Tamenori Y, Ohigashi T, Suga H, Wakabayashi D, Verdier-Paoletti M, Mostefaoui S, Montagnac G, Barosch J, Kamide K, Shigenaka M, Bejach L, Matsumoto M, Enokido Y, Noguchi T, Yurimoto H, Nakamura T, Okazaki R, Naraoka H, Sakamoto K, Connolly HC Jr, Lauretta DS, Abe M, Okada T, Yada T, Nishimura M, Yogata K, Nakato A, Yoshitake M, Iwamae A, Furuya S, Hatakeda K, Miyazaki A, Soejima H, Hitomi Y, Kumagai K, Usui T, Hayashi T, Yamamoto D, Fukai R, Sugita S, Kitazato K, Hirata N, Honda R, Morota T, Tatsumi E, Sakatani N, Namiki N, Matsumoto K, Noguchi R, Wada K, Senshu H, Ogawa K, Yokota Y, Ishihara Y, Shimaki Y, Yamada M, Honda C, Michikami T, Matsuoka M, Hirata N, Arakawa M, Okamoto C, Ishiguro M, Jaumann R, Bibring J-P, Grott M, Schröder S, Otto K, Pilorget C, Schmitz N, Biele J, Ho T-M, Moussi-Soffys A, Miura A, Noda H, Yamada T, Yoshihara K, Kawahara K, Ikeda H, Yamamoto Y, Shirai K, Kikuchi S, Ogawa N, Takeuchi H, Ono G, Mimasu Y, Yoshikawa K, Takei Y, Fujii A, Iijima Y, Nakazawa S, Hosoda S, Takahiro I, Hayakawa M, Sawada H, Yano H, Tsukizaki R, Ozaki M, Terui F, Tanaka S, Fujimoto M, Yoshikawa M, Saiki T, Tachibana S, Watanabe S, and Tsuda Y (2023) Macromolecular organic matter in samples of the asteroid (162173) Ryugu. *Science* 379:eabn9057. <https://doi.org/10.1126/science.abn9057>
- Yada T, Abe M, Okada T, Nakato A, Yogata K, Miyazaki A, Hatakeda K, Kumagai K, Nishimura M, Hitomi Y, Soejima H, Yoshitake M, Iwamae A, Furuya S, Uesugi M, Karouji Y, Usui T, Hayashi T, Yamamoto D, Fukai R, Sugita S, Cho Y, Yumoto K, Yabe Y, Bibring J-P, Pilorget C, Hamm V, Brunetto R, Riu L, Lourit L, Loizeau D, Lequertier G, Moussi-Soffys A, Tachibana S, Sawada H, Okazaki R, Takano Y, Sakamoto K, Miura YN, Yano H, Ireland TR, Yamada T, Fujimoto M, Kitazato K, Namiki N, Arakawa M, Hirata N, Yurimoto H, Nakamura T, Noguchi T, Yabuta H, Naraoka H, Ito M, Nakamura E, Uesugi K, Kobayashi K, Michikami T, Kikuchi H, Hirata N, Ishihara Y, Matsumoto K, Noda H, Noguchi R, Shimaki Y, Shirai K, Ogawa K, Wada K, Senshu H, Yamamoto Y, Morota T, Honda R, Honda C, Yokota Y, Matsuoka M, Sakatani N, Tatsumi E, Miura A, Yamada M, Fujii A, Hirose C, Hosoda S, Ikeda H, Iwata T, Kikuchi S, Mimasu Y, Mori O, Ogawa N, Ono G, Shimada T, Soldini S, Takahashi T, Takei Y, Takeuchi H, Tsukizaki R, Yoshikawa K, Terui F, Nakazawa S, Tanaka S, Saiki T, Yoshikawa M, Watanabe S, and Tsuda Y (2021) Preliminary analysis of the Hayabusa2 samples returned from C-type asteroid Ryugu. *Nature Astron* 6:214–220. <https://doi.org/10.1038/s41550-021-01550-6>
- Yamamoto M (1992) Fractionation of azarenes during oil migration. *Org Geochem* 19:389–402. [https://doi.org/10.1016/0146-6380\(92\)90007-K](https://doi.org/10.1016/0146-6380(92)90007-K)
- Yamashita Y, Naraoka H (2014) Two homologous series of alkylpyridines in the Murchison meteorite. *Geochem J* 48:519–525. <https://doi.org/10.2343/geochemj.2.0340>
- Yokoyama T, Nagashima K, Nakai I, Young ED, Abe Y, Aléon J, Alexander CM, Amari S, Amelin Y, Bajo K, Bizzarro M, Bouvier A, Carlson RW, Chaussidon M, Choi B-G, Dauphas N, Davis AM, Di Rocco T, Fujiya W, Fukai R, Gautam I, Haba MK, Hibiya Y, Hidaka H, Homma H, Hoppe P, Huss GR, Ichida K, Iizuka T, Ireland TR, Ishikawa A, Ito M, Itoh S, Kawasaki N, Kita NT, Kitajima K, Kleine T, Komatani S, Krot AN, Liu M-C, Masuda Y, McKeegan KD, Morita M, Motomura K, Moynier F, Nguyen A, Nittler L, Onose M, Pack A, Park C, Pianì L, Qin L, Russell SS, Sakamoto N, Schönbächler M, Tafla L, Tang H, Terada K, Terada Y, Usui T, Wada S, Wadhwa M, Walker RJ, Yamashita K, Yin Q-Z, Yoneda S, Yui H, Zhang A-C, Connolly HC Jr, Lauretta DS, Nakamura T, Naraoka H, Noguchi T, Okazaki R, Sakamoto K, Yabuta H, Abe M, Arakawa M, Fujii A, Hayakawa M, Hirata N, Hirata N, Honda R, Honda C, Hosoda S, Iijima Y, Ikeda H, Ishiguro M, Ishihara Y, Iwata T, Kawahara K, Kikuchi S, Kitazato K, Matsumoto K, Matsuoka M, Michikami T, Mimasu Y, Miura A, Morota T, Nakazawa S, Namiki N, Noda H, Noguchi R, Ogawa N, Ogawa K, Okada T, Okamoto C, Ono G, Ozaki M, Saiki T, Sakatani N, Sawada H, Senshu H, Shimaki Y, Shirai K, Sugita S, Takei Y, Takeuchi H, Tanaka S, Tatsumi E, Terui F, Tsuda Y, Tsukizaki R, Wada K, Watanabe S, Yamada M, Yamada T, Yamamoto Y, Yano H, Yokota Y, Yoshihara K, Yoshikawa M, Yoshikawa K, Furuya S, Hatakeda K, Hayashi T, Hitomi Y, Kumagai K, Miyazaki A, Nakato A, Nishimura M, Soejima H, Suzuki A, Yada T, Yamamoto D, Yogata K, Yoshitake M, Tachibana S, and Yurimoto H (2022) Samples returned from the asteroid Ryugu are similar to Ivuna-type carbonaceous meteorites. *Science*. <https://doi.org/10.1126/science.abn7850>

## Publisher's Note

Springer Nature remains neutral with regard to jurisdictional claims in published maps and institutional affiliations.

Submit your manuscript to a SpringerOpen® journal and benefit from:

- Convenient online submission
- Rigorous peer review
- Open access: articles freely available online
- High visibility within the field
- Retaining the copyright to your article

Submit your next manuscript at ► [springeropen.com](https://www.springeropen.com)